

# AD-A258 299 DOCUMENTATION PAGE



Form Approved  
OMB No. 0704-0188

Information is estimated to average 1 hour per response, including the time for reviewing instructions, searching existing data sources, gathering and reviewing the collection of information, and completing and reviewing this burden estimate or any other aspect of this collection of information, including the review of existing material in the collection, and to the Office of Management and Budget, Paperwork Reduction Project (0704-0188), Washington, DC 20503.

1. AGENCY USE ONLY (Leave blank)		2. REPORT DATE 1992		3. REPORT TYPE AND DATES COVERED THESIS/DISSERTATION	
4. TITLE AND SUBTITLE Analysis and Comparisons of Inverted Meridional Winds From Space-Borne Measurements of [OI] 5577Å				5. FUNDING NUMBERS	
6. AUTHOR(S) Patrick Neal Purcell, Captain					
7. PERFORMING ORGANIZATION NAME(S) AND ADDRESS(ES) AFIT Student Attending: University of Michigan				8. PERFORMING ORGANIZATION REPORT NUMBER AFIT/CI/CIA- 92-083	
9. SPONSORING / MONITORING AGENCY NAME(S) AND ADDRESS(ES) AFIT/CI Wright-Patterson AFB OH 45433-6583				10. SPONSORING / MONITORING AGENCY REPORT NUMBER	
11. SUPPLEMENTARY NOTES					
12a. DISTRIBUTION / AVAILABILITY STATEMENT Approved for Public Release IAW 190-1 Distribution Unlimited ERNEST A. HAYGOOD, Captain, USAF Executive Officer				12b. DISTRIBUTION CODE	
13. ABSTRACT (Maximum 200 words)					
<div data-bbox="282 1338 649 1581" data-label="Text"> <p><b>DTIC</b> <b>ELECTE</b> <b>DEC 10 1992</b> <b>S A D</b></p> </div>					
14. SUBJECT TERMS				15. NUMBER OF PAGES 67	
				16. PRICE CODE	
17. SECURITY CLASSIFICATION OF REPORT		18. SECURITY CLASSIFICATION OF THIS PAGE		19. SECURITY CLASSIFICATION OF ABSTRACT	
				20. LIMITATION OF ABSTRACT	

## GENERAL INSTRUCTIONS FOR COMPLETING SF 298

The Report Form SF 298 is used for reporting on research and development. It is important that this information be consistent with the rest of the report, particularly the cover and title page. Instructions for filling in each block of the form follow. It is important to **stay within the lines** to meet optical scanning requirements.

### Block 1. Agency Use Only (Leave blank)

**Block 2. Report Date.** Full publication date including day, month, and year, if available (e.g. 1 Jan 88). Must cite at least the year.

**Block 3. Type of Report and Dates Covered** State whether report is interim, final, etc. If applicable, enter inclusive report dates (e.g. 10 Jun 87 - 30 Jun 88).

**Block 4. Title and Subtitle.** A title is taken from the part of the report that provides the most meaningful and complete information. When a report is prepared in more than one volume, repeat the primary title, add volume number, and include subtitle for the specific volume. On classified documents enter the title classification in parentheses.

**Block 5. Funding Numbers.** To include contract and grant numbers; may include program element number(s), project number(s), task number(s), and work unit number(s). Use the following labels:

<b>C</b> - Contract	<b>PR</b> - Project
<b>G</b> - Grant	<b>TA</b> - Task
<b>PE</b> - Program Element	<b>WU</b> - Work Unit Accession No

**Block 6. Author(s).** Name(s) of person(s) responsible for writing the report, performing the research, or credited with the content of the report. If editor or compiler, this should follow the name(s).

**Block 7. Performing Organization Name(s) and Address(es).** Self-explanatory.

**Block 8. Performing Organization Report Number.** Enter the unique alphanumeric report number(s) assigned by the organization performing the report.

**Block 9. Sponsoring/Monitoring Agency Name(s) and Address(es).** Self-explanatory.

**Block 10. Sponsoring/Monitoring Agency Report Number.** If known.

**Block 11. Supplementary Note.** Enter information not included elsewhere such as Prepared in cooperation with... Trans. of... To be published in... When a report is revised, include a statement whether the new report supersedes or supplements the older report.

### Block 12a. Distribution/Availability Statement.

Denotes public availability or limitations. Cite any availability to the public. Enter additional limitations or special markings in all capitals (e.g. NOFORN, REL, ITAR).

**DOD** - See DoDD 5230.24, "Distribution Statements on Technical Documents."

**DOE** - See authorities.

**NASA** - See Handbook NHB 2200.2.

**NTIS** - Leave blank.

### Block 12b. Distribution Code.

**DOD** - Leave blank.

**DOE** - Enter DOE distribution categories from the Standard Distribution for Unclassified Scientific and Technical Reports.

**NASA** - Leave blank.

**NTIS** - Leave blank.

**Block 13. Abstract.** Include a brief (**Maximum 200 words**) factual summary of the most significant information contained in the report.

**Block 14. Subject Terms.** Keywords or phrases identifying major subjects in the report.

**Block 15. Number of Pages.** Enter the total number of pages.

**Block 16. Price Code.** Enter appropriate price code (**NTIS only**).

**Blocks 17. - 19. Security Classifications.** Self-explanatory. Enter U.S. Security Classification in accordance with U.S. Security Regulations (i.e., UNCLASSIFIED). If form contains classified information, stamp classification on the top and bottom of the page.

**Block 20. Limitation of Abstract.** This block must be completed to assign a limitation to the abstract. Enter either UL (unlimited) or SAR (same as report). An entry in this block is necessary if the abstract is to be limited. If blank, the abstract is assumed to be unlimited.

**ABSTRACT:**  
**ANALYSIS AND COMPARISONS OF INVERTED MERIDIONAL**  
**WINDS FROM SPACE-BORNE MEASUREMENTS OF [OI] 5577 Å**

by

Patrick Neal Purcell, Capt, USAF

A thesis submitted in partial fulfillment  
of the requirement for the degree of  
Master of Science  
(Atmospheric and Space Sciences)  
in the University of Michigan  
1992  
(67 pp)

Advisor:

Professor, Timothy L. Killeen

Accepted For	
NTIS	DTIC
DTIC	DTIC
Unannounced	
Justification	
By	
Distribution	
Availability	
Dist	
A-1	

92-31248



7788



The University of Michigan  
Department of Atmospheric, Oceanic and Space Sciences  
Space Physics Research Laboratory

**ANALYSIS AND COMPARISONS OF INVERTED MERIDIONAL  
WINDS FROM SPACE-BORNE MEASUREMENTS OF [OI] 5577 Å**

by

Patrick Neal Purcell

Advisor:

Professor, Timothy L. Killeen



**ANALYSIS AND COMPARISONS OF INVERTED MERIDIONAL  
WINDS FROM SPACE-BORNE MEASUREMENTS OF [OI] 5577 Å**

by

**Patrick Neal Purcell**

**A thesis submitted in partial fulfillment  
of the requirement for the degree of  
Master of Science  
(Atmospheric and Space Sciences)  
in the University of Michigan  
1992**

**Advisor:**

**Professor, Timothy L. Killeen**

© Patrick Neal Purcell 1992  
All Rights Reserved

## ABSTRACT

This thesis provides a database comparison and analysis of daytime lower thermospheric (E-region) inverted meridional winds. This inversion technique was previously developed (Nardi, 1991) to retrieve the true wind at altitude from [OI] 5577 Å measurements from the DE-2 Satellite's Fabry-Perot Interferometer.

The inversion technique is briefly discussed in this study. The raw DE-2 satellite data is processed to obtain spectrograms. This data is processed further to obtain brightness and line-of-sight winds and wind errors. For daytime 5577 Å emissions, these line-of-sight winds are averages over two emission layers. The purpose of the inversion technique is to "unaverage" these winds through an onion peel method on the brightnesses and through a least squares fit to Chapman layers on the volume emission rates.

A data base of forty-four daytime orbits was processed through the inversion technique. These orbits were then compared to two models. The Vector Spherical Harmonic (VSH) model uses output from the National Center for Atmospheric Research - Thermospheric General Circulation Model (NCAR-TGCM) to produce thermospheric winds. The Horizontal Wind Model (HWM) uses both empirical data and a limited set of spherical harmonics to produce thermospheric winds. The output from both models was compared to the inverted wind data to analyze for accuracy and for evidence of gravity wave or tidal activity. Comparisons were also performed for specific latitudes and geomagnetic conditions.

Vertical profiles were also produced comparing the green line (5577 Å) derived meridional winds below 200 km to the red line (6300 Å) winds at

higher altitudes. Again, possible gravity wave and tidal influences were investigated.

## **ACKNOWLEDGEMENTS**

Many people made this masters thesis possible. First of all, thanks goes to the U.S. Air Force who has sponsored me through this program and who now allows me to leave active duty. It is this ability to plan and achieve long-term strategies that provides us all with confidence in the U.S. Defense Department.

Secondly, a note of gratitude to my advisor Dr. Timothy Killeen for his guidance and excellent teaching in this field. Also thanks to Dr. Alan Burns for assistance in producing research products. A special appreciation goes to AFIT students Jerry Davis, Tom Smith, Ed Hume, Steve Quigley, and to Steve Carr for moral support during my last harrowing days on active duty.

The staff here at U of M made the road to a degree much easier. Thanks to Gerry Schmitt for keeping the computers in line and on line, to Mike Minnock for his vast computer knowledge, and to Nelly DeMaldonado, who is by far the best secretary and hardest worker I've ever met.

Lastly thanks goes long distance to family and friends in Atlanta. To Pat and Jeanne Freeman (& Daniel) and to, of course, mom.

## TABLE OF CONTENTS

### Abstract

### Acknowledgements .....i

### 1. Introduction

#### 1.1 General .....1

#### 1.2 The Lower Thermosphere.....2

### 2. The DE-2 Fabry-Perot Interferometer

#### 2.1 Introduction: Dynamics Explorer Overview .....3

#### 2.2 The Fabry-Perot Interferometer.....6

#### 2.3 The Interferometer .....8

#### 2.4 DE - FPI Viewing Geometry.....12

### 3. Greenline - [OI] 5577 Å Emission

#### 3.1 Origin of [OI] 5577 Å.....14

##### 3.1.1 5577 Å Nightglow.....14

##### 3.1.2 5577 Å Twilight/Dayglow .....15

##### 3.1.3 5577 Å Aurora .....18

#### 3.2 Variability of [OI] 5577 Å.....19

<b>4. Brightness Inversion</b>	
4.1 Onion Peel Inversion.....	21
4.1.1 Inversion Method .....	21
4.1.2 Inversion Results .....	23
4.2 Least Squares Fit Inversion.....	26
4.2.1 Inversion Method .....	26
4.2.2 Inversion Results .....	28
4.3 Summary and Comparisons .....	30
<b>5. Wind Inversion</b>	
5.1 Inversion Algorithm.....	32
5.2 Wind Inversion - Weighted/Constrained.....	34
<b>6. Comparison to Model Winds</b>	
6.1 The Vector Spherical Harmonic (VSH) Model.....	38
6.2 Comparisons with VSH Model Winds.....	40
6.3 Comparisons with HWM Model Winds.....	43
<b>7. Altitudinal Profiles</b>	
7.1 Red/Green line profile comparisons.....	46
<b>8. Discussion</b> .....	53
<b>Appendix A Thesis sub-topic: Impact ionization</b> .....	55
<b>References</b> .....	64

## CHAPTER 1

### INTRODUCTION

#### 1.1 General

This thesis follows a doctoral thesis that derived an inversion technique to recover lower thermospheric meridional winds from remote measurements of atomic oxygen 5577 Å emission (Nardi, 1991). The objective here is to assemble a data base of these winds and compare them to model output and to red line (6300 Å) winds from the same instrument.

Most of the inverted wind data presented here will be daytime/twilight winds. The inversion technique is not necessary for nighttime measurements since only one emission altitude exists at night.

Measuring the lower thermospheric winds has been a problem in the 5577 Å range due to a double layer in the day time. The satellite measures the total emission from both layers, but cannot distinguish the amount contributed to the total from each layer. Nardi (1991) has developed a method using a fit to Chapman layers that allows for the first time the lower daytime thermospheric winds to be accurately derived from satellite measurements.

The meridional winds are then compared to the output from the Vector Spherical Harmonic (VSH) Model and the Horizontal Wind Model (HWM). These models are presented with the inverted meridional winds for evidence of gravity wave and tidal effects.

The inverted meridional winds are also plotted with higher altitude red line (6300 Å) winds. The red line winds require no inversion process and were measured in an alternating mode (with the green line) by the satellite late in the Dynamics Explorer mission.

## 1.2 The Lower Thermosphere

The lower thermosphere and upper mesosphere remain the least understood regions of the atmosphere. These altitudes are too low for in-situ satellite measurements and too high for tropospheric type in-situ measurements. Most information is gathered through remote measurements such as meteor radar (radar tracking of meteor trails 80-100 km), MST radar (Mesosphere, Stratosphere, Troposphere; echos VHF signals off an optically clear atmosphere), and Incoherent Scatter Radar that sends UHF pulses into the ionosphere.

The lower thermosphere is affected by forces that are not as important at higher altitudes. More radiative energy is deposited in the lower thermosphere due to a larger optical depth. Tides and gravity waves are also a major energy source as they propagate upward from lower altitudes and deposit energy as they break in this region.

## CHAPTER 2

### THE DE-2 FABRY-PEROT INTERFEROMETER

#### 2.1 Introduction: Dynamics Explorer Overview

The Dynamics Explorer (DE) program was a National Aeronautics and Space Administration (NASA) sponsored launch of two spacecraft to study the coupling between the magnetosphere, ionosphere and the atmosphere. The DE spacecraft were launched during the summer of 1981 and relayed data until February 1983. DE project scientists decided that two satellites were necessary; one satellite at a low altitude orbit and the other at a high altitude orbit. The satellites were launched into coplanar orbits within common magnetic flux tubes. This configuration allowed measurements from the magnetosphere and the ionosphere/atmosphere at the same time. The DE mission had four objectives that were not covered in previous programs (Hoffman, et. al., 1981). They were:

- (1) Measurements of the three-component dc electric fields with global coverage.
- (2) Measurements of the velocity vector of the neutral winds in the upper ionosphere.

(3) Measurements of magnetic fields, plasmas, particle distribution functions, neutral gas parameters, characteristic light emissions, and plasma waves, along with neutral wind velocities and electric fields.

(4) Measurements of field and plasma parameters at both high and low altitudes within the same magnetic flux tube.

The instruments on the DE spacecraft were grouped into five categories of measurement : thermal ions, thermal neutral particles, suprathermal particles, fields, and optical remote sensing. The Fabry-Perot Interferometer is a remote optical sensing instrument and was a new technique for spaceborne measurements when the DE spacecraft were launched. Most other instruments were adapted from the Atmospheric Explorer (AE) program or the International Sun Earth Explorer (ISEE) program.

The primary investigators for each instrument are listed in table 2-1. These instruments are able to measure the following:

- thermal electrons
- thermal ions
- thermal neutral particles
- suprathermal particles
- vector magnetic field
- vector electric field
- plasma waves
- auroral optical images
- Very Low Frequency (VLF) transmissions over Antarctica

TABLE 2-1

Dynamics Explorer Investigators		
L.H.Brace	Goddard Space Flight Center	Langmuir Probe
J.L.Burch	Southwest Research Institute	High Altitude plasma instrument
G.R.Carignan	University of Michigan	Neutral mass spectrometer
C.R. Chappell	Marshall Space Flight Center	Retarding ion mass spectrometer
F.V.Coroniti	University of California, Los Angeles	Theoretical Program
L.A.Frank	University of Iowa	Global auroral imager
W.B.Hanson	University of Texas at Dallas	Ion drift meter
P.B.Hays	University of Michigan	Fabry-Perot interferometer
R.A.Heelis	University of Texas at Dallas	Ion drift meter
R.A.Helliwell	Stanford University	Controlled and naturally occurring wave-particle interactions analysis
R.A.Hoffman	Goddard Space Flight Center	Low altitude plasma analysis
N.C.Maynard	Goddard Space Flight Center	Vector electric field instrument
H.G.Mayr	Goddard Space Flight Center	Theoretical program
A.F. Nagy	University of Michigan	Theoretical Program
R.G.Roble	National Center for Atmospheric Research	Theoretical Program
E.G.Shelley	Lockheed Palo Alto Research Laboratory	Energetic ion mass spectrometer
S.D.Shawhan	University of Iowa	Plasma wave instrument
N.W.Spencer	Goddard Space Flight Center	Wind and Temperature Spectrometer
M.Sugiura	Goddard Space Flight Center	Magnetometers
J.D.Winningham	Southwest Research Institute	Low altitude plasma instrument

The apogee and perigee altitudes were designed to be high enough for auroral viewing, plasmasphere and plasmopause observations near the equator, and wave and particle measurements in the magnetosphere. These high altitude measurements were all made from the high altitude spacecraft.

From the low altitude spacecraft measurements needed to be under 300 km for neutral particle and thermospheric wind measurements.

Measurements were also needed above 1000 km for interaction of suprathermal ions and the atmosphere. The actual altitude range of the lower altitude satellite was approximately 200 km to 1000 km.

The ground data system for the DE mission was designed to give the investigators access to the information as quickly as possible. DE scientists used the same system that the Atmospheric Explorer mission used. This consisted of a Science Data Processing System at Goddard Space Flight Center. A central computer facility processed the majority of the data at Goddard with remote terminals at the investigator's facilities.

## 2.2 The Fabry-Perot Interferometer

The Fabry-Perot Interferometer (FPI) on the Dynamics Explorer is a highly stable single etalon interferometer with optics able to view the atmosphere at various tangent heights. A single Doppler profile (spectral and spatial scan) gives us the temperature, meridional wind, and density of any one of several excited atoms or ions in the thermosphere. These Doppler profiles are measured with a resolution of  $10^{-4}$  Å. Table 2-2 lists the species and spectral regions of measurement.

One of the major goals of the DE mission was to increase our knowledge of thermospheric wind and temperature fields. How heat enters and leaves (is deposited and dissipated) the thermosphere is not well understood due simply to lack of data. We do know that heat enters this region by solar UV radiation, magnetospheric energy (particle or joule heating near the magnetic poles, and wave or tidal energy transported from

**TABLE 2-2**  
Emissions measured by FPI

Species	Spectral Region	Value
O( <sup>1</sup> D)	6300 Å	Upper thermosphere wind and temperature
O+( <sup>2</sup> P)	7320 Å	Upper thermosphere ion drift and temperature
O( <sup>1</sup> S)	5577 Å	Mesospheric nighttime neutral winds and lower thermospheric daytime winds
N( <sup>2</sup> D)	5200 Å	Auroral energy storage
Na( <sup>2</sup> P)	5896 Å	Mesospheric neutral wind and temperature daytime

lower altitudes. How much each of these contributes and how their contributions fluctuate with changing geophysical conditions is still unknown.

The Fabry-Perot interferometer is shown in figure 2.1. There are three sections to the instrument: the telescope section, the mirror section, and the interferometer section. The telescope consists of the main objective doublet lens (that is, two lenses of differing shapes) and the main baffle. The instrument collects light originating from 25 - 225 km (tangent point altitudes) below the satellite. The FPI is restricted to looking along the satellite's line-of-sight. The light enters the baffle and stray light from the Earth's or Sun's bright limb or from cloud tops on the day-side is

eliminated by this baffle. The lens forms a vertical slice image of the sky by focusing the collected light onto the sky stop.

This vertical slice then enters the mirror section. This section contains the horizon scan mirror that is a concave, front surfaced mirror that pivots. This mirror reflects and refocuses light from the sky stop to the field stop. The scan mirror selects different circular elements from our vertical slice of sky. The pivoted position of the mirror determines which vertical segment of the sky is focused onto the field stop.

The field stop is a circular aperture at the exit of the mirror section. This aperture blocks unwanted portions of the image from entering the etalon of the FPI and allows a small sector to pass through.

### 2.3 The Interferometer

The interferometer section of the FPI consists of a collimator telescope lens, a dielectric blocker, a schott glass blocker, a filter, the high resolution etalon, a focusing telescope lens and the image plane detector. Specifics on the filter wheel and the scan mirror are listed in table 2-3. The emitted light passes through the field stop and is collimated and filtered for the desired wavelength. This light then passes through the etalon. The etalon is made of two fused silica plates separated and held parallel by the three spacing elements. Each plate is coated with several semi-reflective layers. Light passes through the first plate and some light is reflected back from the second plate while the rest passes on through. This interference creates a phase shift in the light that creates a unique "fingerprint" or spectrogram determined by the intensity and wavelength of

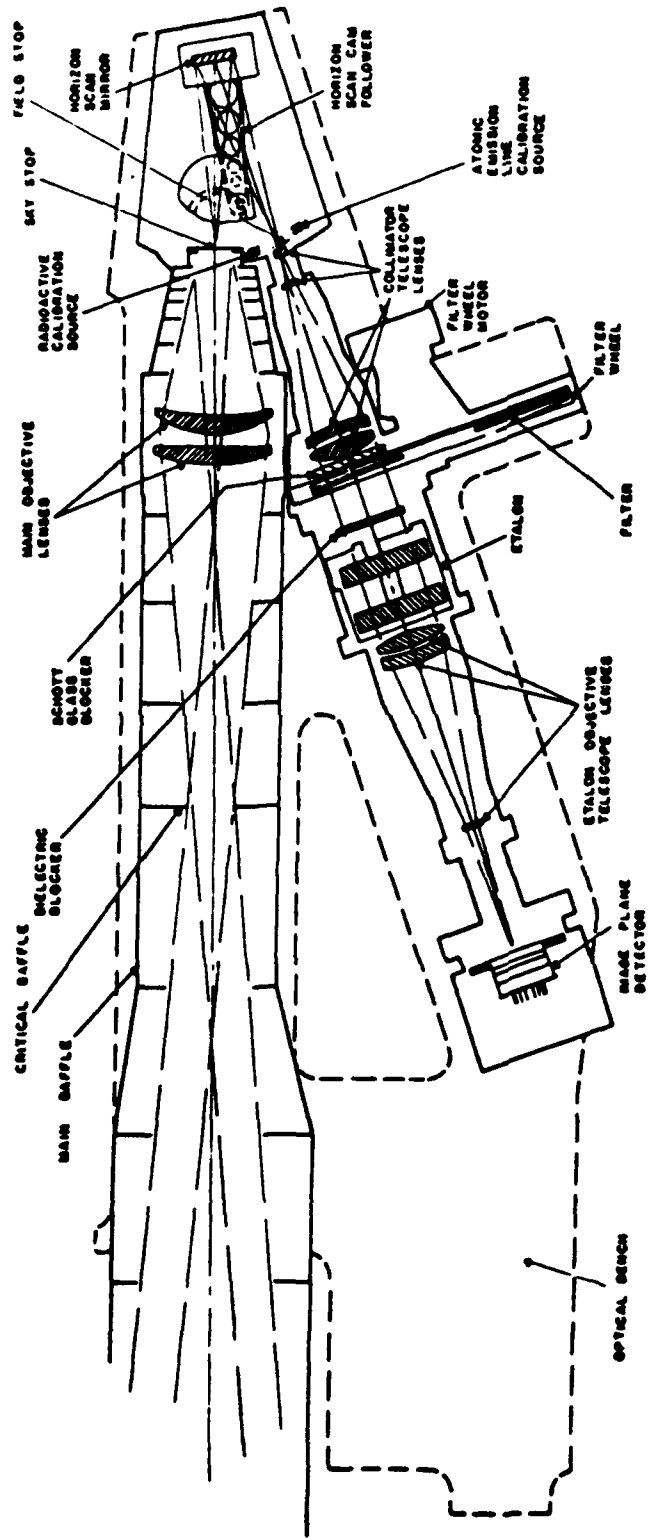


figure 2.1 Optical schematic for the Fabry-Perot Interferometer (Hays et. al., 1981).

**TABLE 2-3****FPI Filter Wheel and Scan Mirror Specifications**

<b><u>Filter Wheel:</u></b>	<ol style="list-style-type: none"> <li>1) Fixed filter: any one of eight possible filter positions</li> <li>2) Filter cycling: the filter wheel may be stepped at the following rates:               <ol style="list-style-type: none"> <li>a) once per <math>2^n * 0.5</math> s (<math>n=0-7</math>) in fast (default) mode</li> <li>b) once per <math>2^n * 0.5</math> s (<math>n=3-7</math>) in slow (backup) mode</li> </ol> </li> <li>3) Filter sequencing: the filter wheel may be commanded to alternate between any two filter positions</li> <li>4) Impulsive go step (automatic filter sequence) if logic is lost.</li> </ol>
<b><u>Scan Mirror:</u></b>	<ol style="list-style-type: none"> <li>1) Fixed mirror: any one of 16 sky positions and 2 calibration positions</li> <li>2) Scan mirror cycling: the mirror may be stepped once per <math>(2^n * 0.25) + 0.25</math> s (<math>n=0-7</math>)</li> <li>3) Impulsive go step (automatic scan sequence) if logic is lost</li> </ol>

the light. The etalon transforms the spectral distribution of an emission line into a radial distribution in the form of a circular fringe pattern. This circular pattern is what the image plane detector measures.

The image plane detector (IPD) converts the light intensity distribution of the interference fringe into discreet electron pulses. These pulses are measured a segmented anode made up of 12 concentric rings of equal area. The measured output of each anode ring corresponds to one of

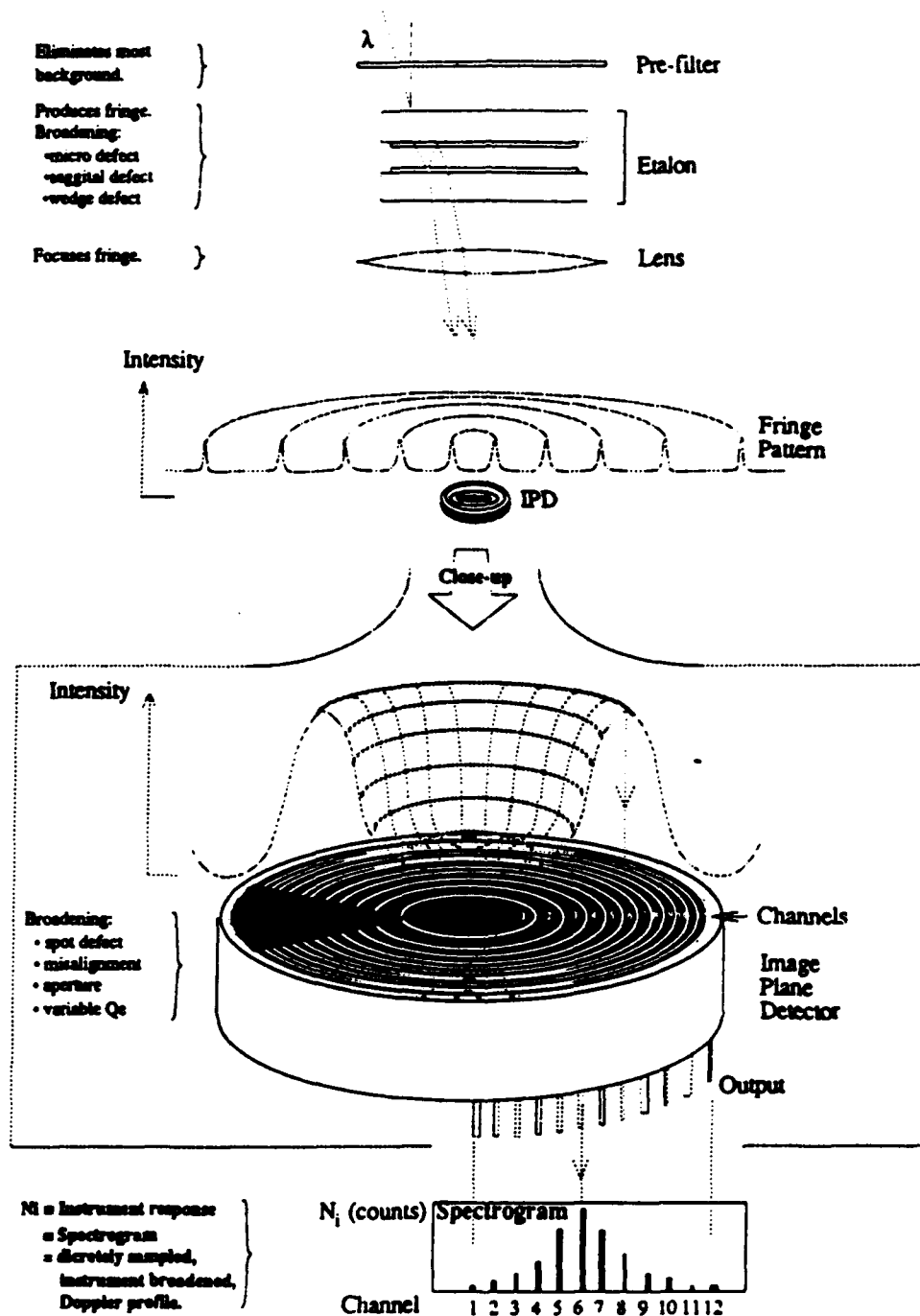


figure 2.2 The multi-channel detector's measurement of the fringe pattern produced by the etalon. One radial 'cut' of one order of the fringe will produce a spectrogram that gives wind and temperature information. The multi-channel detector samples the entire fringe simultaneously for greater resolution.

12 channels on a spectrogram. Figure 2.2 illustrates this concept. From these spectrograms we can extract wind, temperature, and brightness information.

#### 2.4 DE - FPI Viewing Geometry

The sixteen sky positions of the horizon scan mirror allow a scan from  $5^{\circ}$  -  $15^{\circ}$  below the spacecraft's local horizontal (tangent to the Earth). Figure 2.3 is a schematic showing the viewing geometry of the FPI and DE satellite. The tangent point is the point along the line of sight view of the FPI where the line of sight is tangent to a shell concentric with the surface of the earth. This height happens to be the altitude where the contribution to any FPI measurement is at a maximum. This is because the path length of the line-of-sight is longest through a layer centered at the tangent point.

The tangent heights range from ~25 - 225 kilometers below the satellite altitude. The instrument axis is an imaginary line passing through all of the optical surfaces of the instrument. The instrument axis lies  $10.294^{\circ}$  below the local horizontal for the majority of the DE-2 mission.

Finally, the view axis is the same as the line-of-sight and varies from  $5^{\circ}$  -  $15^{\circ}$  below the local horizontal. This is the imaginary line that passes through the centroid field-of-view for any viewing position.

## Satellite Measurement Geometry: DE2-FPI

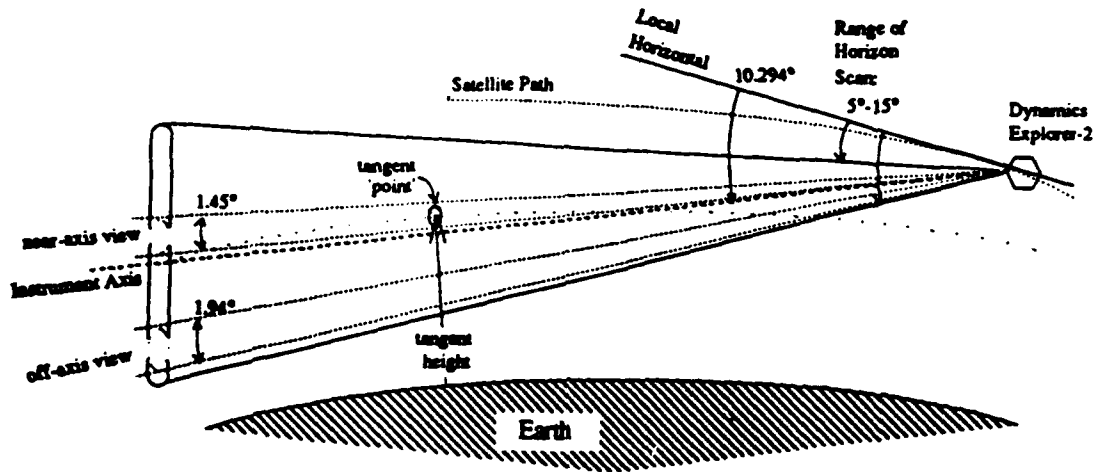


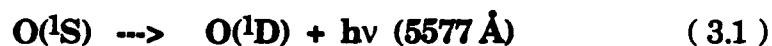
figure 2.3 DE2-FPI viewing geometry. This schematic shows the instrument axis, the range of the horizon scan and the varying field-of-view for the DE2-FPI.

## CHAPTER 3

## GREENLINE - OI 5577 Å EMISSION

## 3.1 Origin of [OI] 5577 Å

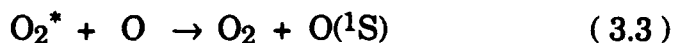
The 5577 Å emission originates from the  $^1S \rightarrow ^1D$  electric quadrupole transition of atomic oxygen:



## 3.1.1 5577 Å Nightglow

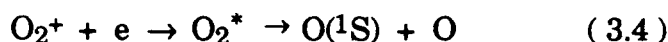
The OI 5577Å nightglow has two layers; one at  $97 \pm 2$  km and an upper layer at approximately 240 km. The upper layer is one order of magnitude dimmer than the lower layer (Cogger and Anger, 1973). The peak volume emission rate of the upper layer is 3 - 4 photons  $\text{sec}^{-1} \text{ cm}^{-3}$  compared to 50 - 360 photons  $\text{sec}^{-1} \text{ cm}^{-3}$  for the lower layer.

For the lower layer (< 120 km) the product of  $O(^1S)$  is thought now to be due to the Barth mechanism:

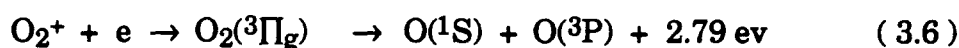
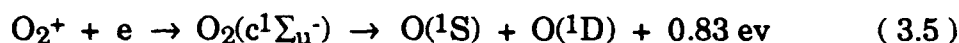


where the  $O_2^*$  is most likely  $O_2(c^1\Sigma_u^-)$  (Bates, 1988).

For the upper layer dissociative recombination is the source of O(<sup>1</sup>S) green line airglow:



The O<sub>2</sub><sup>\*</sup> can be produced in one of two ways:

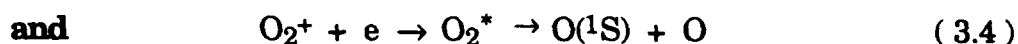
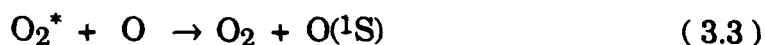
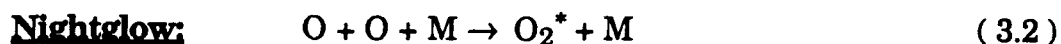


The question as to which of these branches is primarily responsible for the production of O(<sup>1</sup>S) is still under study. Branching ratio studies were performed (Hernandez, 1971) using ground based Fabry-Perot interferometer data. These studies suggested equation ( 3.6 ). The problem with this study, however, is that the upper layer of 5577Å emission is masked by the brighter lower layer emission at 97 km.

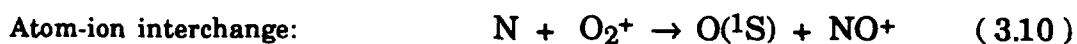
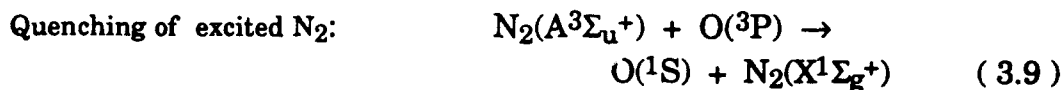
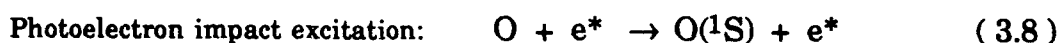
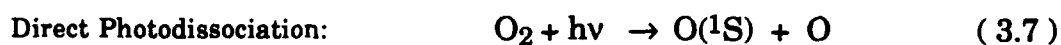
Killeen and Hays ( 1981 ) used DE2-FPI data from the DE2 satellite to obtain accurate branching ratio values. Their results favored equation ( 3.5 ). The recombination reaction that leads to the production of O(<sup>1</sup>S) is dependent on the electron temperature ( Zipf, 1988 ) and density (Abreu et al., 1983) as well as the vibrational distribution of O<sub>2</sub><sup>+</sup> (Guberman, 1979; Zipf, 1979, 1980). Inconsistences arise in the populations and collisional frequencies of O<sub>2</sub><sup>+</sup>.

### 3.1.2 5577Å Twilight/Dayglow

Sources for the 5577Å dayglow are the same as for the nighttime sources plus others as summarized below:



**Others:**



All of these sources are significant in twilight airglow. Which source is dominant depends upon the altitude.

The lower layer at ~100 km is still present in the twilight and daytime airglow, but is somewhat thicker than at night. This is due to reaction (3.7), the production of  $O(^1S)$  through direct dissociation of molecular oxygen. This is the dominant reaction above 260 km and significant above 190 km.

There is also an upper layer in twilight, but the peak is lower than at night. In fact, the upper layer is highest at night (~240 km) and descends in altitude with decreasing solar zenith angle as daytime conditions develop. The twilight altitude of the upper layer is ~200-220 km and the daytime peak is at ~160-170 km. The intensity of the upper layer, however, increases from 3-4 photons  $\text{sec}^{-1} \text{cm}^{-3}$  at night to ~10-60 photons  $\text{sec}^{-1} \text{cm}^{-3}$

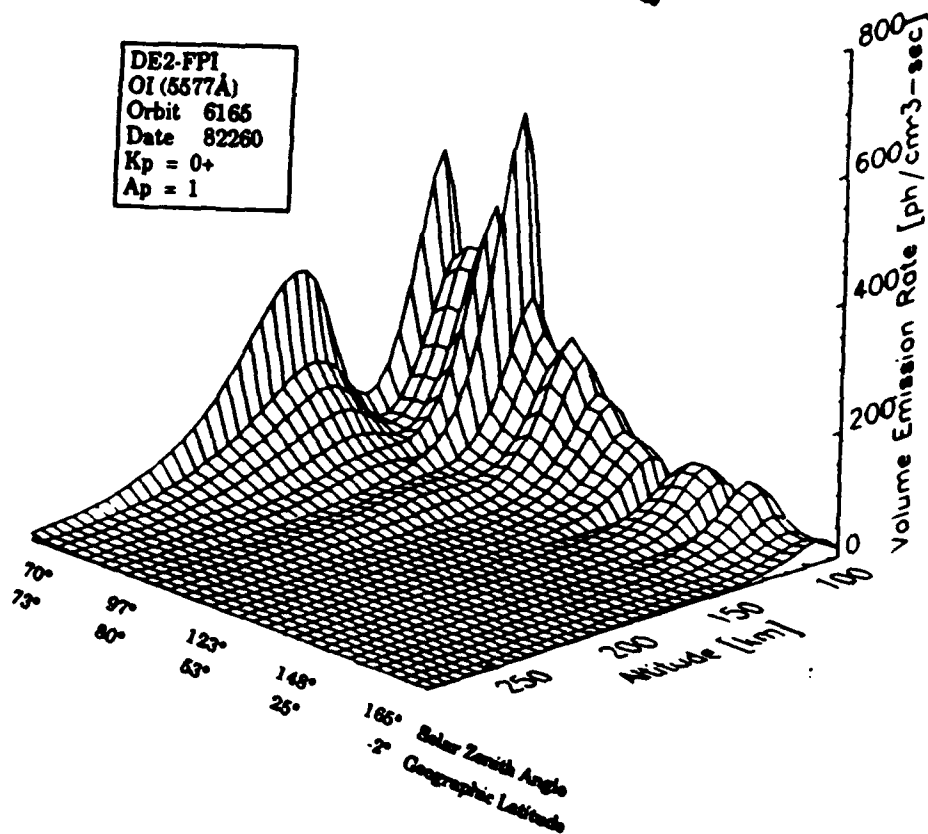
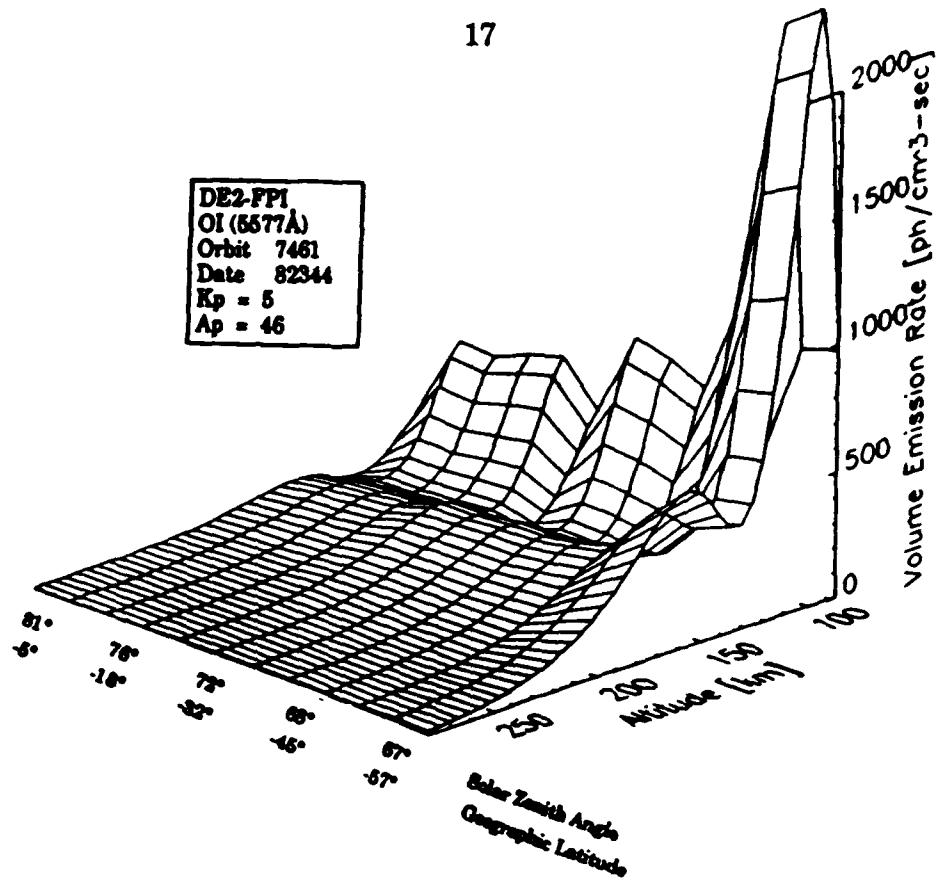


figure 3.1 Volume emission rates from orbits 7461 and 6165. Two layers of emission can be seen, one at 97 km and one at ~160 km. The upper layer decreases in intensity and raises in altitude with increasing solar zenith angle.

for twilight to  $\sim 120\text{-}200$  photons  $\text{sec}^{-1} \text{cm}^{-3}$  in dayglow. Figure 3.1 shows two surface plots of volume emission rates as a function of angle along track (or latitude) and altitude. From these plots it is evident that there are two layers of emission and that the upper layer increases in intensity as daytime conditions develop and decreases with increasing solar zenith angle.

These plots do not show the change in altitude of the upper layer very well because they have constrained the volume emission rates to two specific altitudes, 97 and 160 km. These constrained volume emission rates will be discussed in detail in the next chapter.

### 3.1.3 5577Å Aurora

The emission of [OI] 5577Å during aurora is extremely variable in intensity and altitude. Because of this, its sources are difficult to determine. Whereas the nightglow intensity is  $\sim 60\text{-}250$  Rayleighs (lower layer) and the dayglow intensity is  $\sim 200\text{-}1000$  Rayleighs, the auroral 5577Å emission is  $\sim 500\text{-}7000$  Rayleighs with a peak at 105 km (Sharp et al., 1979; Solomon 1987).

Much study has been accomplished to determine which reaction is the dominant source of the emission with significant uncertainty remaining. Reaction (3.9) is now accepted as the major producer of  $\text{O}(^1\text{S})$  in the aurora (Sharp et al., 1979; McDade and LLewellyn, 1984b, 1985). Other reactions have been considered, but are thought to be only minor sources of  $\text{O}(^1\text{S})$ .

One other possible reaction still under study is:



This source was suggested by Yau and Shepherd (1979) and could be a major source below 105 km. Here, the  $\text{O}_2^*$  is probably  $\text{O}_2(^1\Sigma_u^-)$  from auroral high energy electrons (Solheim and LLewellyn, 1979).

### 3.2 Variability of [OI] 5577 Å

The latitudinal, seasonal, diurnal and solar-cycle variations in the [OI] 5577 Å are quite pronounced. Before any analysis of lower thermospheric winds can be performed, a basic understanding of these variations is necessary.

The *seasonal variation* appears to be semiannual in nature. The maximum emissions were found to be just after equinoxes (April - May, October - November) and minimum emissions were just after the solstices (January - February, July - August). Smith and Steiger (1968) found a variation factor of 6 in from  $\sim 20^\circ$  to  $32^\circ$  N latitude.

Subsequent ground based and satellite studies have confirmed that this semiannual variation is somewhat dependent on latitude with minimum variations at the geographic equator and maximum variations from  $40^\circ$  to  $60^\circ$  in both hemispheres.

The *diurnal variation* is semidiurnal just as the seasonal variation was semiannual. Studies have shown a maximum increase of 50-100% in the 5577 Å intensity in this semidiurnal variation caused by the semidiurnal solar tide. The maximum ranges in local solar time

anywhere from 22 - 06 LST. The exact time depends on the month and latitude but still shifts from year to year. It is because of this shifting that long term studies did not yield any clear patterns since the maximums were averaged out and produced no clear daily oscillation.

The *solar cycle/geomagnetic variation* is most apparent from 30° to 60° latitude. This variation does seem to be dependent on solar cycle/solar sunspot number. The variation is also dependent on the orientation of the interplanetary magnetic field (IMF) with an increase of nightglow measurements under positive IMF conditions and decreased intensities under negative IMF conditions.

*Small Scale Variations* are evident in the measurements as a result of gravity waves and tides. Waves are anywhere from 6-250 km with transverse lengths as high as hundreds of kilometers.

## CHAPTER 4

### BRIGHTNESS INVERSION

#### 4.1 Onion Peel Inversion

##### 4.1.1 Inversion Method

The idea behind the 'onion peel' method is to 'peel' away brightness measurements from upper atmospheric layers successively to reveal contributions from lower layers. We assume or know nothing about the amount of contribution these lower layers might yield before performing the inversion. Altitude-scanned limb brightness measurements are used from the DE2-FPI. An inversion algorithm solves for the inverted or 'onion peeled' volume emission rate by relating the height integrated volume emission rate to the limb-scanned brightness measurements.

In terms of an equation:

$$B(z_t) = \int_z K(z, z_t) \eta(z) dz \quad (4.1)$$

$B(z_t)$  = Surface brightness at tangent height  $z_t$

$\eta$  = Volume emission rate profile (function of altitude ,  $z$ )

$K(z, z_t)$  = Brightness Inversion kernel:

$$K(z_t, z) = \sum_{i=1}^{12} K_{A/F_i}(z_t, z) \quad (4.2)$$

$K_{A/F_i}$  = Altitude broadening kernels for the individual ring anodes , channels 1-12 from the FPI image plane detector. These kernels are functions of the field-of-view weighting functions from raytrace simulations. These raytrace simulations were necessary to correct for distortions produced by the FPI's optics. The raytrace takes an individual ray of light from its emission source in the atmosphere and follows it through the FPI optical components to where it strikes the optical sensor of the FPI (see figure 2.1).

To actually perform calculations using equation 4.1, it must first be represented in matrix form:

$$[B] = [K][\eta] \quad (4.3)$$

Here,  $[B]$  and  $[\eta]$  are column vectors ( $N \times 1$ ) and  $[K]$  is an  $N \times N$  matrix. The next step is to invert the  $[K]$  matrix to get the solution  $[\eta]$ :

$$[\eta] = [K]^{-1} [B] \quad (4.4)$$

This, however, is best done by using singular value decomposition (SVD). SVD rewrites or 'decomposes' the  $[K]$  matrix into three other matrices:

$$[K] = [U] [W] [V]^T \quad (4.5)$$

Where  $[U]$  is the eigenvector matrix of  $[K]$  and  $[V]$  is the eigenvector matrix of  $[K]^T$  and  $[U]$  and  $[V]$  are orthogonal. Performing the inversion

this way helps to deal with singularities or near-singularities in the kernel matrix  $[K]$  by isolating the problems in the eigenvalue matrix  $[W]$ . Since  $[U]$ ,  $[V]$ , and  $[W]$  are all either orthogonal or diagonal, they are much easier to manipulate than the  $[W]$  matrix. The final solution can now be written as:

$$\begin{aligned} [\eta] &= [K]^{-1} [B] = \{[U][W_j][V]^T\}^{-1} [B] \\ &= [V] \cdot [\text{diag}(1/[W_j])] \cdot ([U]^T \cdot [B]) \quad (4.6) \end{aligned}$$

#### 4.1.2 Inversion Results

Figure 4.1 shows the unconstrained brightness inversion profile (plusses). The fit is close to the model brightness everywhere except at large vertical gradients (the E-region layer). Note that in the upper daytime plot the F-region layer is resolved well with this 'onion peel' inversion. The poor resolution of the E-region layer is also evident in the bottom panel where there is no upper F-region emission layer.

Figure 4.2 shows a surface plot of the unconstrained inversion at the top. The bottom surface plot is a 2-layer chapman fit (to be discussed next section). The E-region once again is not as well resolved in the upper plot as it is in the lower chapman layer plot. The reason for this is that the chapman layer inversion constrains the emission layers to specific altitudes with specific half-thicknesses using a least squares algorithm. This is the topic of the next section.

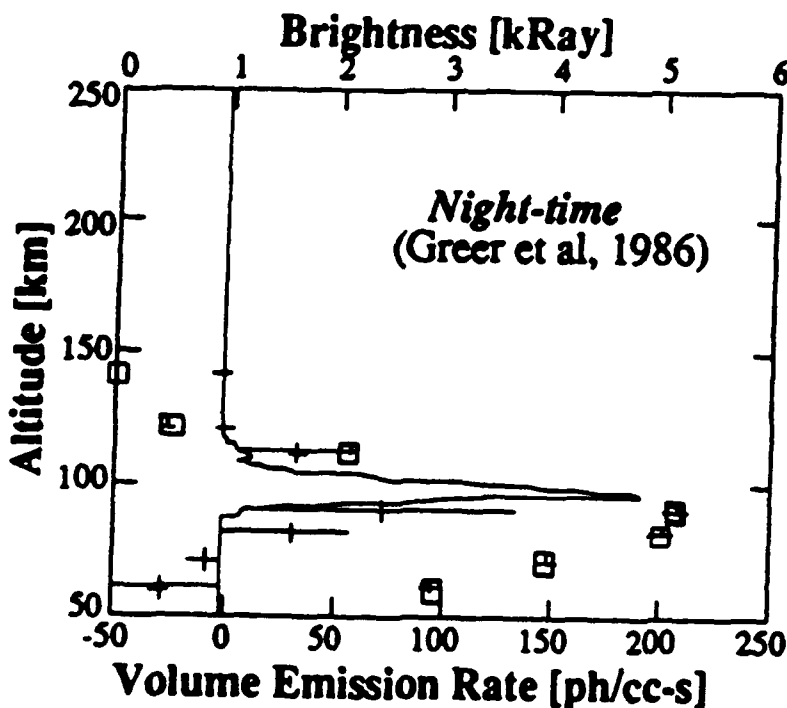
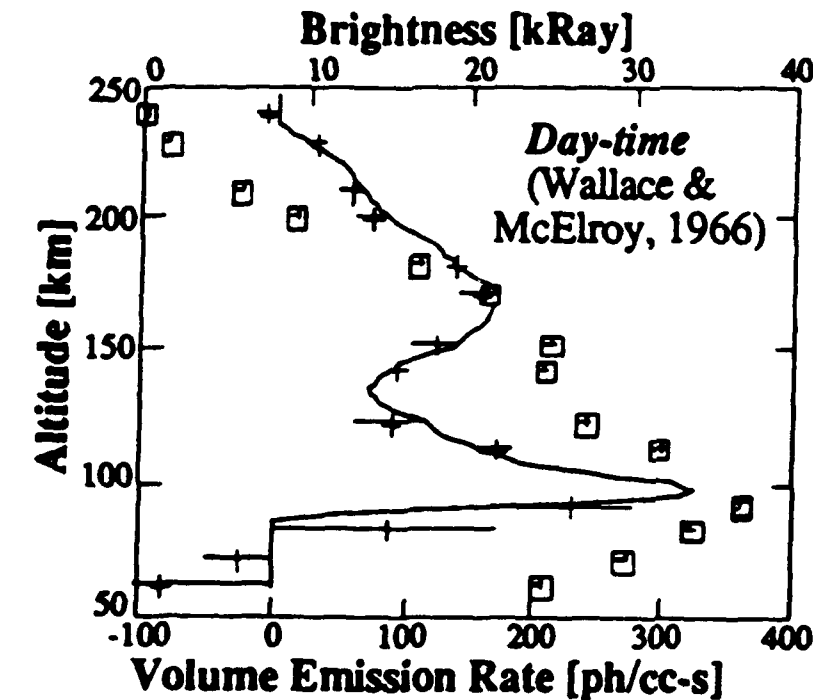


figure 4.1  
'Onion Peel'  
brightness inversion  
for daytime and  
nighttime conditions.  
The line is a plot of a  
model volume  
emission rate, the  
boxes a simulated  
limb brightness  
profile, and plusses  
are the inverted  
volume emission  
rate. The inverted  
inversion rate fits the  
model well where no  
large vertical  
gradients exist. The  
E region peak,  
however, is not  
handled as well by the  
inverted volume  
emission rate where  
there is a large  
vertical gradient due  
to near singularities  
caused by the large  
field of view of the  
DE2-FPI.

□ simulated limb brightness  
+ inverted volume emission rate  
— model volume emission rate

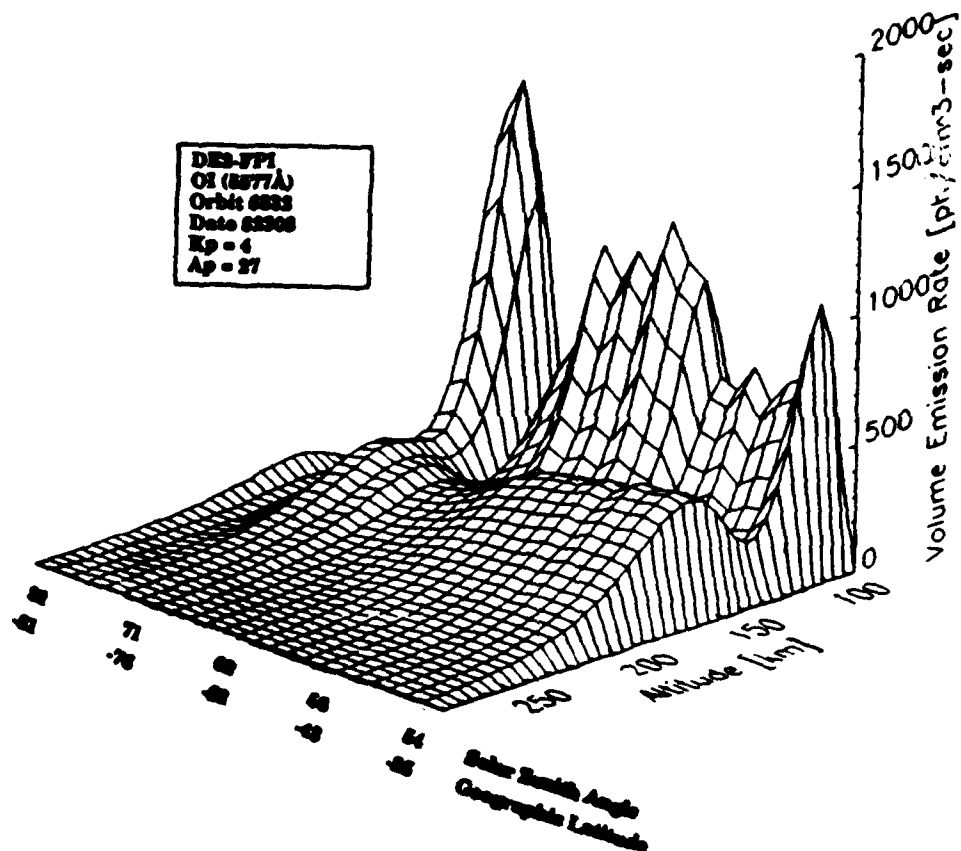
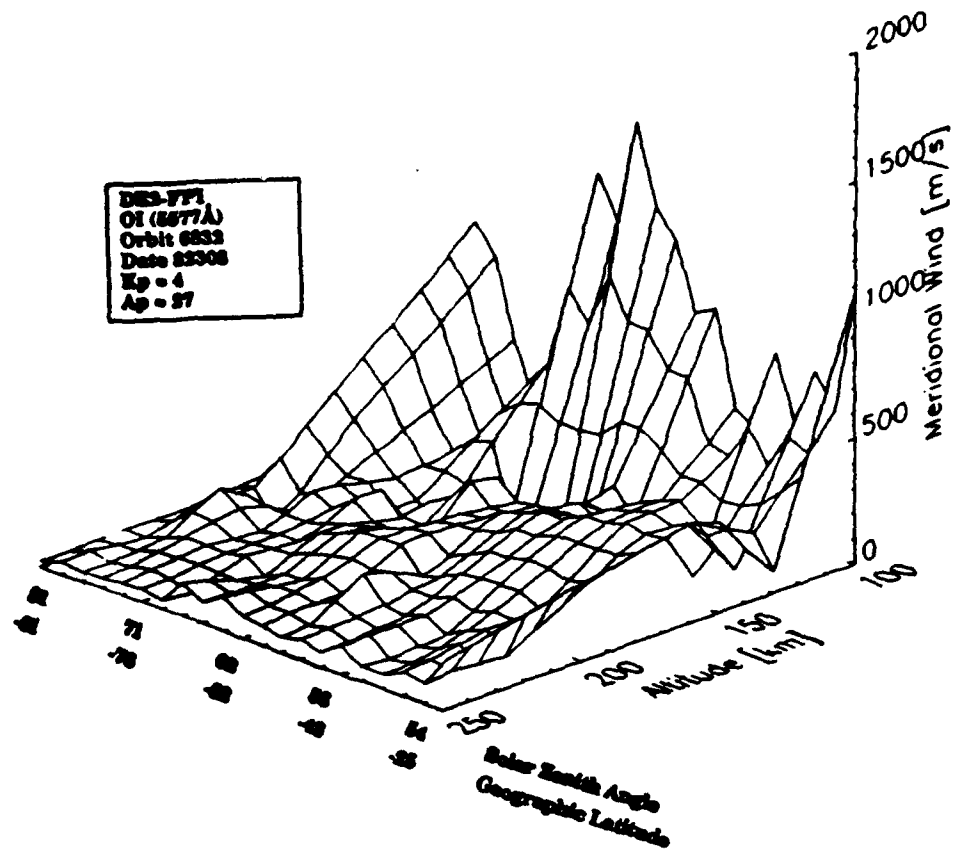


figure 4.2 Brightness inversions for DE2 orbit 6832. The top surface plot shows the unconstrained "onion-peel" inversion while the bottom plot shows the 2-layer chapman fit inversion.

## 4.2 Least Squares Fit Inversion

### 4.2.1 Inversion Method

An alternative to performing an unconstrained inversion is to pre-determine the shape of the volume emission rate profile. The layers of emission are known as Chapman layers with assumed peak heights and half-thicknesses.

From a known Chapman emission layer we produce simulated limb-scan brightness profiles. These simulated profiles are then fitted to DE2-FPI limb-scanned brightness measurements to determine the best Chapman layer characteristics. The volume emission rate profile is obtained by performing a scaled summation of the Chapman emission rate layers.

This chapter will address a two layer Chapman layer, but as many layers as desired can be used (i.e. four, six, ...). The two Chapman layer has the following characteristics:

Region	Peak Emission	Half-thickness
E-Region (night)	97 km	10 km
E-Region (day)	97 km	~25 km
F-Region (night)	200+ km	Variable
F-Region (day)	160 km	Variable

TABLE 4-1

The mathematics behind the inversion begins with the formula for the model Chapman function emission layers:

$$\eta_{ci}(z) = Y_i \exp \left\{ \frac{1}{2} \left[ 1 - \frac{(z - z_{\pi})}{H_{\pi i}} - \frac{1}{\mu_i} \exp \frac{-(z - z_{\theta})}{H_{\theta i}} \right] \right\}, \quad i = 1, 2 \quad (4.7)$$

$\eta_{ci}(z)$  = Volume emission rate for Chapman layer  $i$

$H_{\theta i}$  = Fixed bottom-side scale height

$H_{\pi i}$  = Fixed top-side scale height

$z_i$  = Fixed height of peaks emission

$Y_i$  = Arbitrary magnitude

The simulated limb brightness profile,  $B_{ci}(z_t)$ ,  $i=1,2$ , that matches this model Chapman function is:

$$B_{ci}(z_t) = \int_{\text{FOV}} K(z, z_t) \eta_{ci}(z) dz, \quad i = 1, 2 \quad (4.8)$$

Here  $K(z, z_t)$  is the same brightness kernel as discussed in the last section. The two simulated brightness profiles  $B_{c1}(z_t)$  and  $B_{c2}(z_t)$  are fitted using constants  $X_1$  and  $X_2$  to match as closely as possible (least squares algorithm) the measured DE2-FPI brightness profile  $B(z_t)$  as in:

$$[B_c] \cdot [X] = [B] \quad (4.9)$$

The least squares method is used to obtain the best solution for the modulating constants,  $X_i$ ,  $i=1,2$ . Once these constants are known, the inverted volume emission rate profile is found by calculating the weighted sum of the original Chapman layers from:

$$\eta(z) = X_1 \eta_{c1}(z) + X_2 \eta_{c2}(z) \quad (4.10)$$

In other words, if the  $X_1$  layer had a contribution of 1 and the  $X_2$  layer had a contribution of 2, then the  $\eta_{c2}(z)$  volume emission rate layer would be twice as large as the  $\eta_{c1}(z)$  emission rate layer. Since the  $X$ 's are directly dependent on the Chapman layer form, it is evident that the Chapman layer chosen has a direct effect on the shape of the resulting volume emission rate.

#### 4.2.2 Inversion Results

Figure 4.3 shows the two brightness inversions (unconstrained and 2-layer chapman fit) for orbit 6565. Here it is easier to see the poorer resolution of the E-region by the unconstrained inversion in the top surface plot. The F and E regions are distinguishable, but not to the extent of the chapman inversion shown on the bottom plot. Once again with both plots the F region emission decreases in magnitude as twilight approaches. In the top plot, however, the lift in altitude can also be seen. The chapman inversion cannot show this because we have predetermined the two emission layer's altitudes and these altitudes cannot change without running another inversion with new emission layer altitudes.

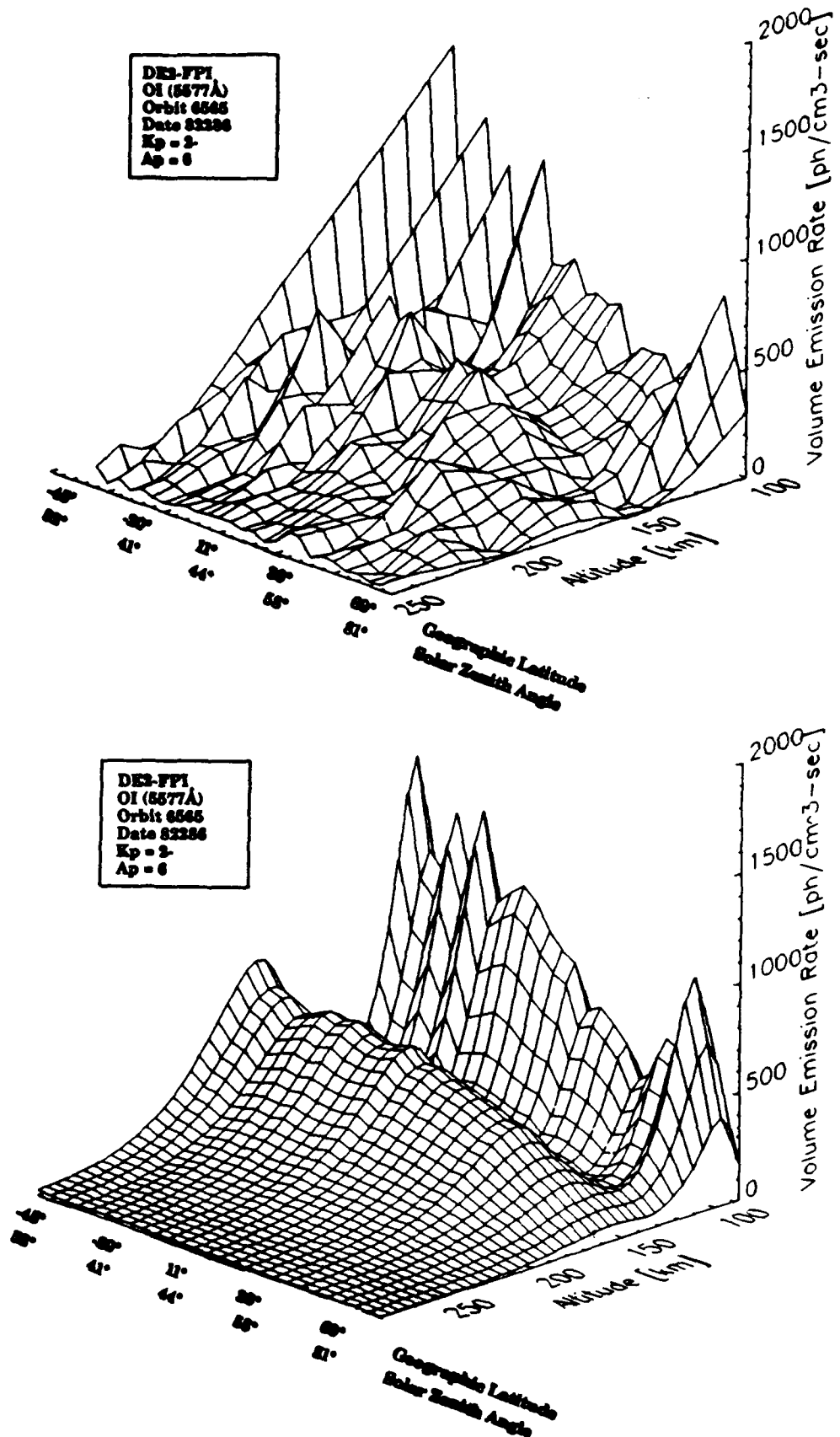


figure 4.3 Brightness inversions for DE2 orbit 6565. The unconstrained inversion is at the top while the 2-layer Chapman fit is at the bottom. The better resolution of the E-region is evident in the Chapman layer fit.

### 4.3 Summary and Comparisons

The following table summarizes the two inversion techniques:

**INVERSION TECHNIQUES**

<u>CONDITION</u>	<u>'ONION PEEL'</u>	<u>2-LAYER CHAPMAN</u>	<u>4-LAYER CHAPMAN</u>
<u>Daytime F-Region (Upper Region)</u>	X		
<u>Daytime E-Region (Lower Region)</u>		X	
<u>Aurora</u>			X
<u>Nighttime</u>		X	
<u>Twilight</u>	X		

**TABLE 4-2**

The night-time inversion is not really needed since the only emission layer is the E-region layer. No upper F-region layer exist to add to the line-of-sight winds, so the actual line-of-sight winds are the actual E-region winds.

The advantages of the chapman layer inversion is that once again the E-region is better resolved. But there are several disadvantages. The main problem is that it is difficult to know the exact height and half-thicknesses of the emission layers. Another problem occurs when the satellite altitude varies more than  $\pm 30$  km. The assumed chapman emission layers are calculated with a fixed satellite altitude in mind. When the actual altitude varies from this altitude too much the accuracy of the fit is compromised. Of course we could just change the reference chapman layer brightness

profiles with changing satellite altitude, but this would introduce much more computational time.

The unconstrained inversion, on the other hand, is less computationally extensive and more desirable even though the E-region is not resolved as well. This inversion also calculates the brightnesses at the tangent heights which is exactly what is required for the wind kernel evaluations. Lastly, the unconstrained inversion gives maximum freedom to the shape of the emission profile. That is, it allows the altitude shift of the emission layers from day to night.

Because of these three advantages, the unconstrained 'onion peel' inversion is used to calculate the wind inversion kernels.

## CHAPTER 5

### WIND INVERSION

#### 5.1 Inversion Algorithm

The wind inversion algorithm is a weighted/constrained inversion. The volume emission rate profiles used to calculate the wind inversion algorithm are acquired from a previous onion peel inversion of brightness measurements as discussed in the previous chapter.

The line-of-sight (LOS) winds are averaged winds over the viewing path of the DE satellite. Figure 5.1 illustrates this concept. To get the actual wind at each altitude, another inversion process must be applied.

The first step is to write an equation that relates the line-of-sight wind to the raw data of the DE2-FPI. This has been done through a simplified variation of a four parameter least squares fit algorithm. After this, a relationship between the line-of-sight winds and the actual winds at height  $z$  must be determined. This involves relating changes in the line-of-sight wind to changes in the response of the channels of the FPI through a least squares method. The changes in the response of the channels of the FPI include the volume emission rate profiles previously obtained (and

# LINE-OF-SIGHT WIND MEASUREMENT: DE-FPI

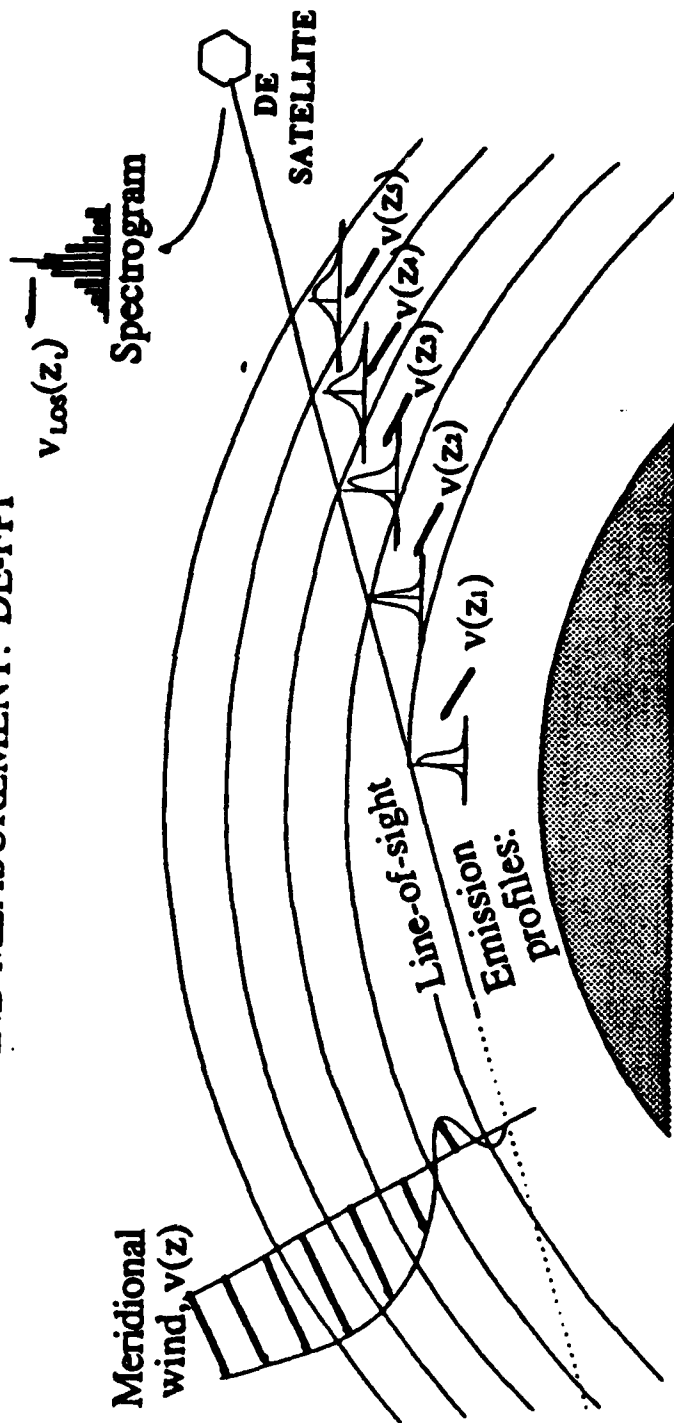


figure 5.1 Drawing showing the constituents of the line-of-sight wind. Each individual spectrogram at a different height is averaged so that the FPI measures a net averaged doppler shift through its line-of-sight. An inversion process is necessary to determine the local wind that produced each unaveraged doppler shift.

associated brightness kernels). The final line-of-sight wind equation can be written:

$$v_{los}(z_t) = \int K'(z, z_t) v(z) dz + v_{los0}(z_t) \quad (5.1)$$

where:

$v_{los}(z_t)$  = Line-of-sight wind at tangent height  $z$

$K'(z, z_t)$  = Wind inversion kernel (includes altitude averaging effect)

$v_{los0}(z_t)$  = Apparent winds - these are artificial winds produced from gradients in the volume emission rate profile

The wind kernel  $K'$  also includes a wind offset factor of 330 m/s for 5577Å emission. This offset is due to technical factors related to how the FPI measures the brightness data.

## 5.2 Wind Inversion - weighted/constrained

This inversion is weighted by a covariance matrix  $S_{v_{los}}$  as shown:

$$v = (\gamma H + K^T S_{v_{los}}^{-1} K)^{-1} (K^T S_{v_{los}}^{-1} v_{los}) \quad (5.2)$$

where:

$v$  = actual wind

$\gamma$  = A weighting factor whose optimal value is 0.003 . This value was determined by testing various combinations of  $\gamma$  and the Nth order difference matrix H.

H = An nth order difference matrix. This difference matrix limits the number of inflection points in the inverted wind profile and here  $n=1$ . The higher the value of n, the less constraint on the solution.

K = The wind inversion kernel

$S_{vlos}$  = The covariance matrix consisting of the line-of-sight wind errors

$v_{los}$  = The line-of-sight winds

The accuracy of the inverted winds using this weighted constrained procedure are +/- 15 m/s with a spatial resolution of +/- 10 km. Figure 5.2 shows inverted winds for three profiles of DE2 orbit. The fine wave structure is evident in the inverted wind, particularly at lower altitudes (~ 100 - 150 km).

Figure 5.3 shows surface plots of the inverted wind for orbits 6565, 6725, and 6745. A definite fine wave structure can be seen both altitudinally and latitudinally. These are probably the results of gravity waves and/or tides propagating from lower altitudes.

# Weighted/Constrained Wind Inversion

## Day-glow

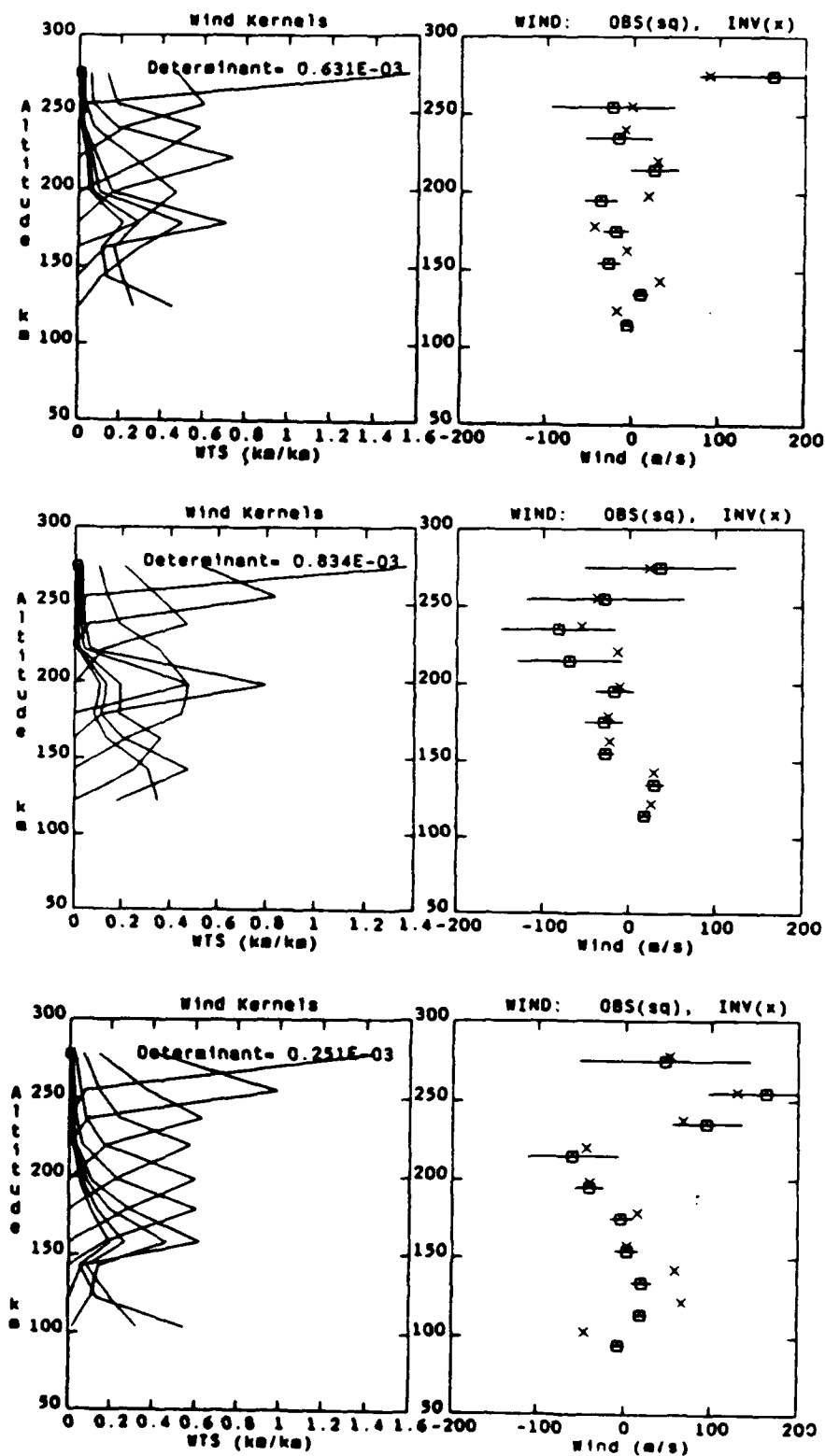


figure 5.2 Three consecutive profiles of DE2 orbit 6565 showing the line-of-sight winds and the inverted winds on the right and associated wind kernels on the left.

# Meridional Winds: Weighted Constrained Inversion

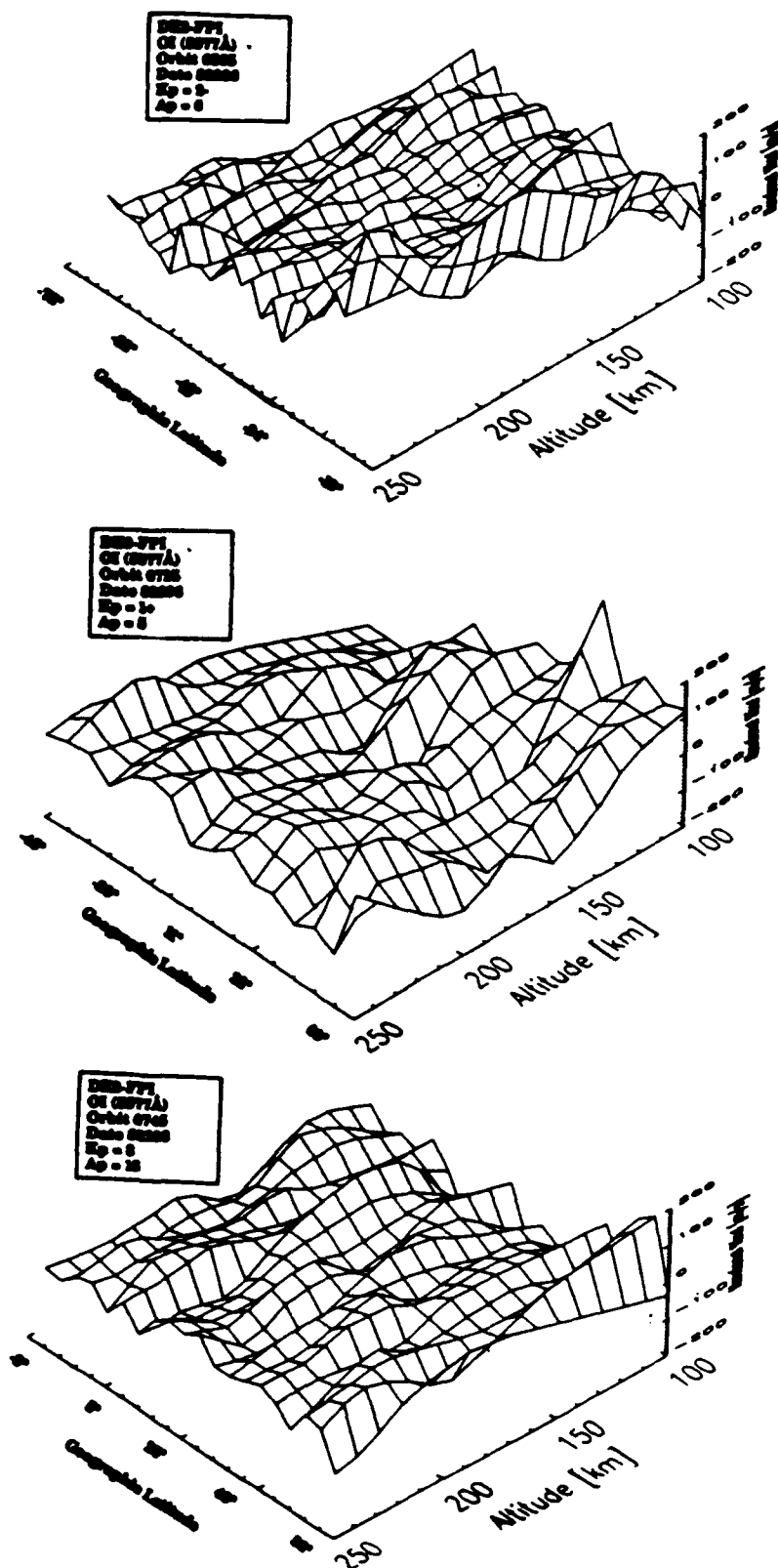


figure 5.3 Three surface plots of the inverted meridional winds from orbits 6565, 6725, and 6745.

## **CHAPTER 6**

### **COMPARISONS TO MODEL WINDS**

#### **6.1 The Vector Spherical Harmonic (VSH) Model**

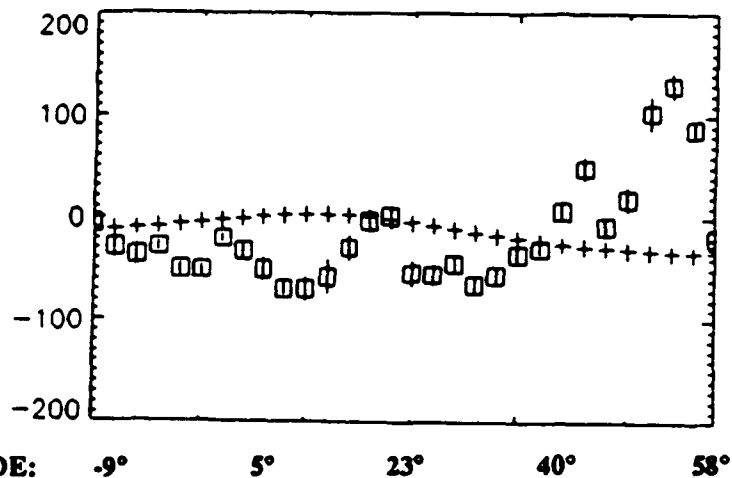
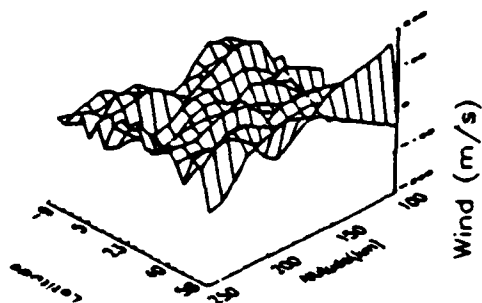
The Vector Spherical Harmonic (VSH) model is a semi-empirical model that uses output from the NCAR-TIGCM. The NCAR-TIGCM (National Center for Atmospheric Research's Thermospheric Ionospheric General Circulation Model) solves the three dimensional time dependent equations that describe the thermosphere.

The VSH model uses TIGCM derived coefficient files. These coefficients are actually weighting factors created from operations on the TIGCM wind, temperature, and composition outputs. This operation is a vector spherical expansion on wind fields and a scalar spherical expansion on the temperature and composition.

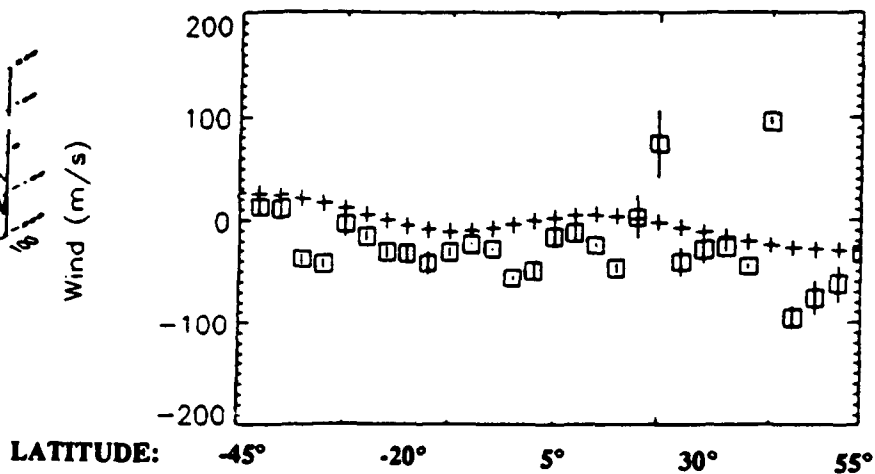
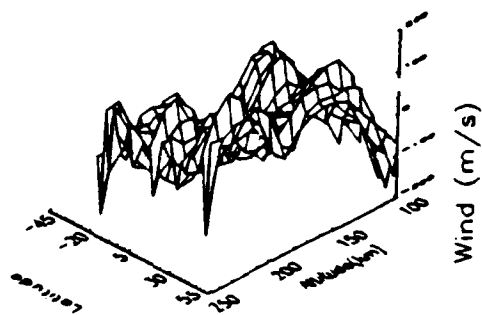
These coefficient files reside in a coefficient library and include a variety of conditions (seasonal variation, magnetic activity, and solar activity). These files total to 18 runs of the TIGCM ready for use by the VSH model.

# INVERTED MERIDIONAL WIND VS VSH WIND - 110 km

ORBIT: 6745  
JDAY: 82298



ORBIT: 6696  
JDAY: 82295



ORBIT: 6681  
JDAY: 82294

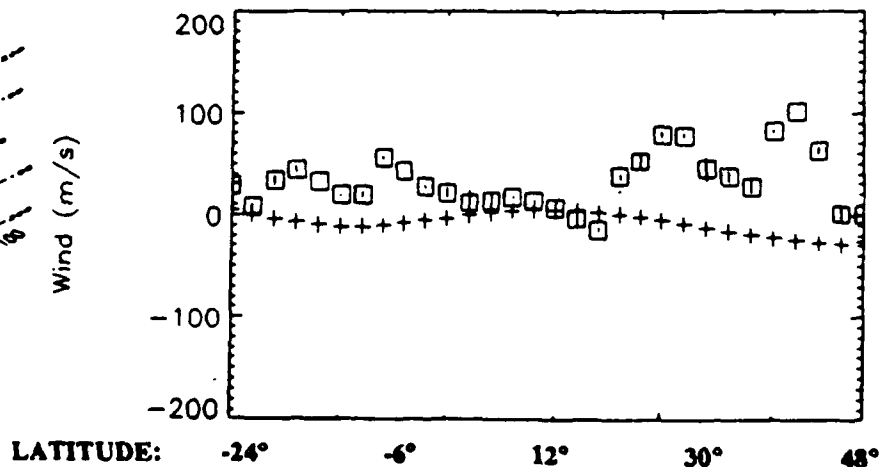
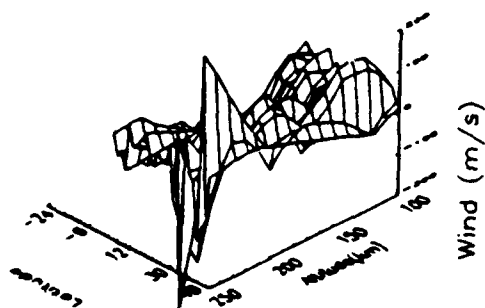


figure 6.1 Three orbits of DE2 showing the surface plot to the left and an altitude slice at 110 km comparing the inverted meridional wind (boxes) to the VSH model wind (plusses).

## 6.2 Comparisons with VSH Model Winds

Figure 6.1 shows altitude slices at 110 km for three DE2 orbits comparing the inverted meridional winds to the VSH winds. It is immediately evident that there is a fine wave structure to the meridional winds that the VSH model is not capable of producing. These waves are the probably the result of gravity waves or tidal motions. The NCAR-TIGCM has been modified to take into account the effects of upward propagating tides in the lower thermosphere ( Fesen et al., 1986). The effect of this modification, however, is limited in the VSH model and shows up as a semidiurnal effect on the meridional wind output. Gravity waves are not well understood and still very difficult to predict or model.

Over forty DE2 orbits were processed to provide inverted meridional green line winds. These winds were binned and averaged by latitude and ap indices and are shown in figure 6.2. The low ap averages show the best correlation to the VSH model meridional winds, especially between  $-45^{\circ}$  and  $45^{\circ}$  latitude. At higher latitudes, auroral effects cause much greater perturbations in the inverted winds.

The medium ap averages also show a good correlation with the model output, except at high latitudes. The high ap VSH output, however, shows a fairly poor match to the inverted winds at all latitudes.

These results are what might be expected given previous studies of the dynamics of the lower thermosphere. Cogger et al. (1985) studied the  $5577\text{\AA}$  emission over Calgary, Canada ( $51^{\circ}$  N,  $114^{\circ}$  W, geographic) using 75 nights of data. He found a highly variable wind field with maximum

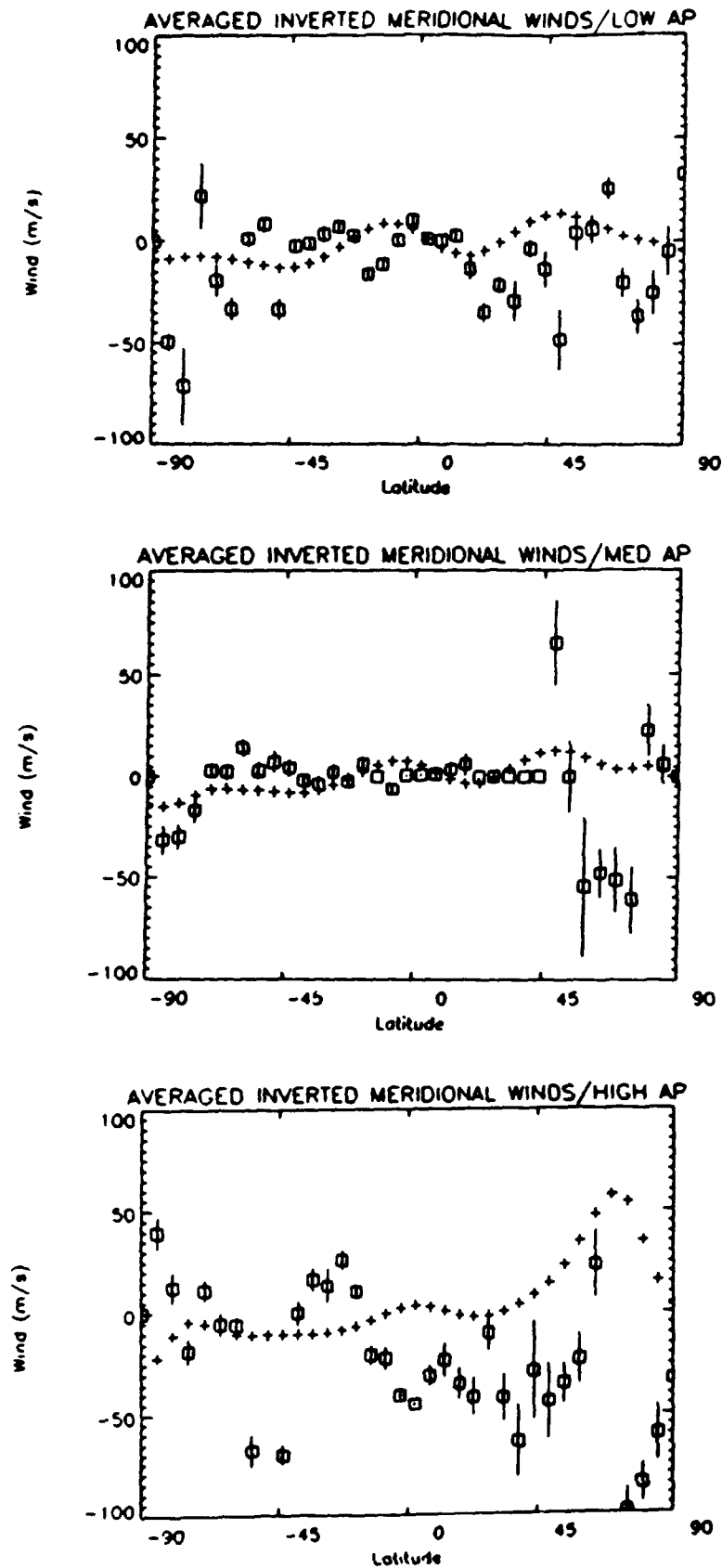
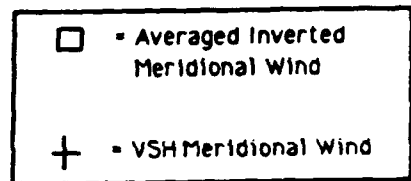


figure 6.2 Comparisons of VSH model meridional wind (plusses) to the averaged inverted meridional wind (boxes) at 110 km. The Low ap at mid and low latitudes shows the best correlation while the high ap at high latitudes shows the worst. The averages are binned over  $10^\circ$  latitude and represent approximately forty DE2 orbits.



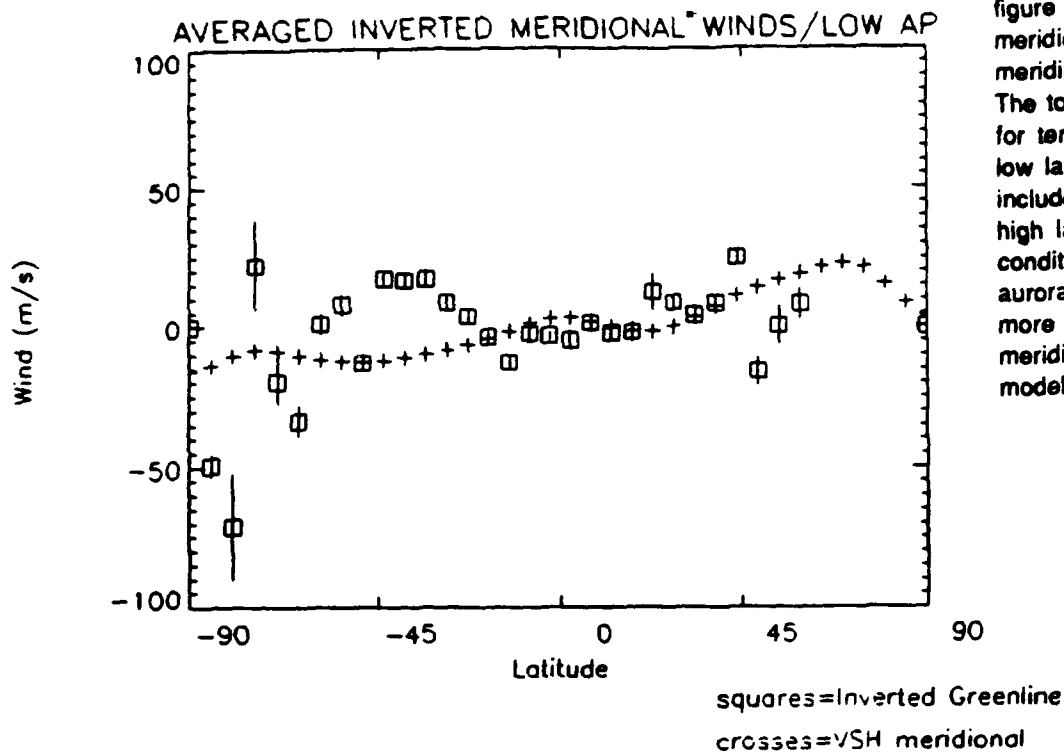
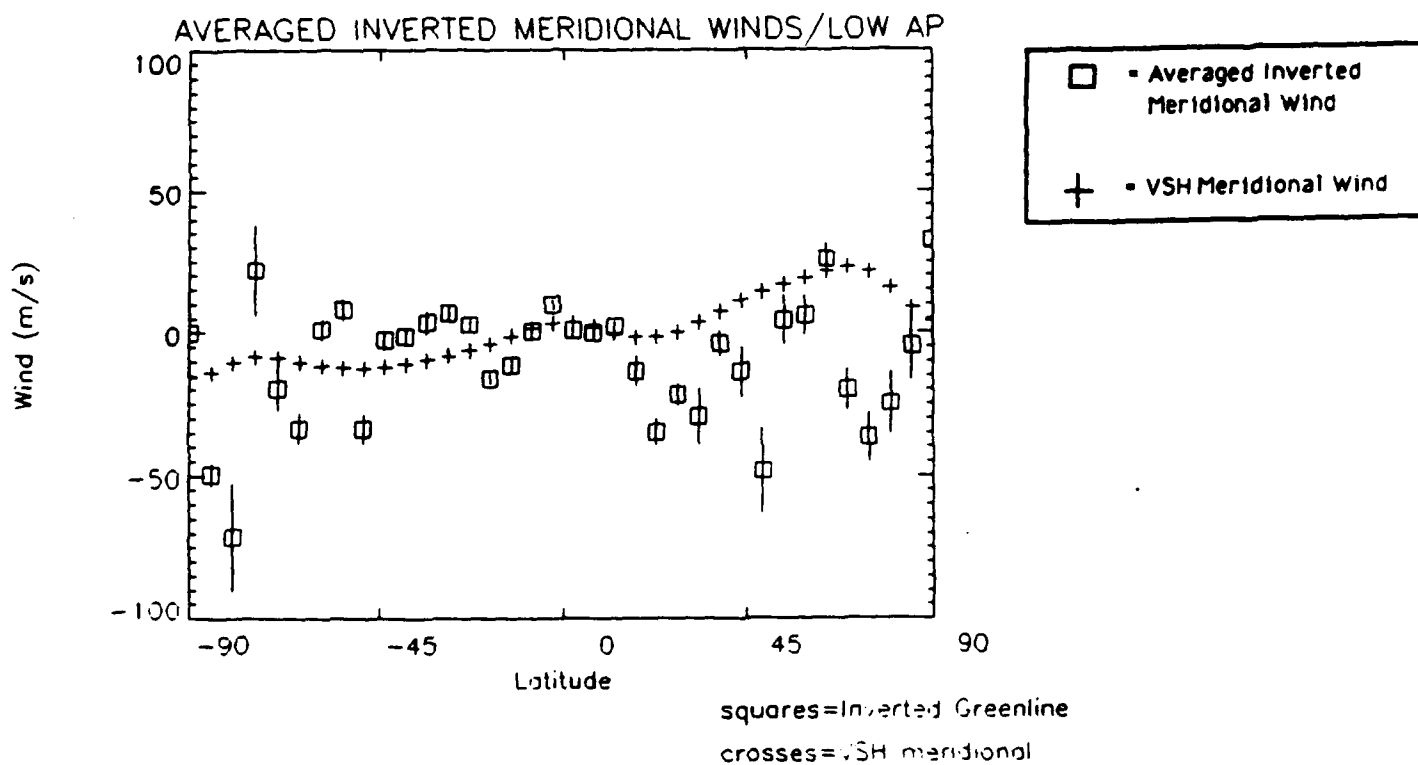


figure 6.3 Averaged low ap meridional winds vs. VSH meridional winds at 110 km. The top plot shows an average for ten orbits mostly at mid and low latitudes. The bottom plot includes twelve more orbits at high latitudes under auroral conditions. In the bottom plot, auroral conditions cause much more variation in the meridional wind that the VSH model cannot match.



speeds near  $200 \text{ ms}^{-1}$  during disturbed geomagnetic periods. At times, stable wind patterns were observed, at other times, little organization was present.

Johnson and Luhmann (1985) studied MST (Mesospheric, Stratospheric, Tropospheric) radar data from Poker Flat, Alaska ( $65^\circ\text{N}$ ). They found the thermospheric winds to be poorly ordered and highly variable in relation to geomagnetic activity. The results presented here seem to be in agreement with these findings.

Figure 6.3 shows two versions of averaged low ap inverted meridional wind. The top plot shows a mixture of all conditions while the bottom plot includes auroral conditions. The variability is greater for auroral conditions as expected, although again the best correlation to the model output occurs at low and mid latitudes.

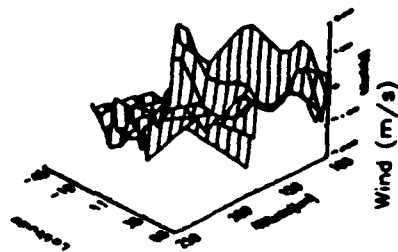
### 6.3 Comparison to the HWM Model

The inverted meridional winds are also compared to the Horizontal Wind Model (HWM90). The HWM90 is a revised version of the HWM87 empirical model (Hedin et al., 1988) that provides upper thermospheric winds based on DE2 and AE-E satellite data. The newer version incorporates ground-based incoherent scatter radar and Fabry-Perot data to extend the lower range of the model from 220 km to 100 km. A limited set of spherical harmonic expansions are used in this model. The HWM provides winds in a manner similar to the MSIS-86 model's output of temperature, density, and composition.

The model agrees well with various data sets, especially at low and mid latitudes (Hedin et al., 1991). Solar activity variations are also included

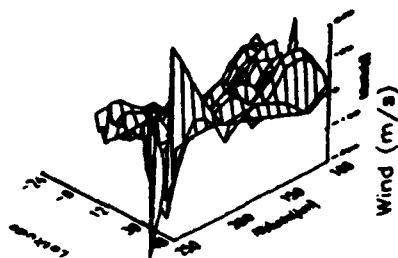
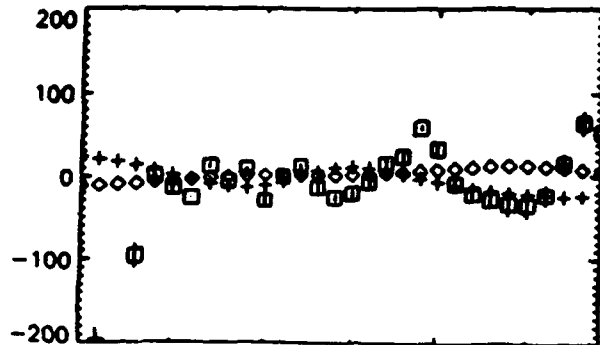
in the model, although they were found to be small. The model describes diurnal variations in the upper thermosphere and semidiurnal variations in the lower thermosphere.

Figure 6.4 shows three orbits of DE2-FPI inverted green line data. The surface plots are shown on the left with an altitude slice plotted at the right. Also plotted are the VSH model meridional winds (plusses) and the HWM model meridional winds (triangles). Consistent with previous findings of the HWM model, the best fit to the inverted winds occur at mid and low latitudes. The VSH and HWM models do not disagree with each other to any great extent, but both clearly miss the effects of gravity waves and tides seen in the inverted winds, especially in orbit 6681.



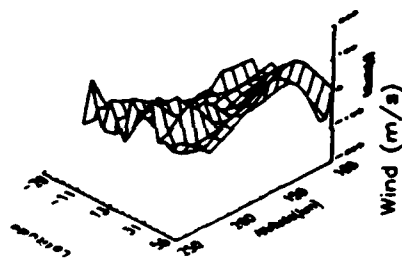
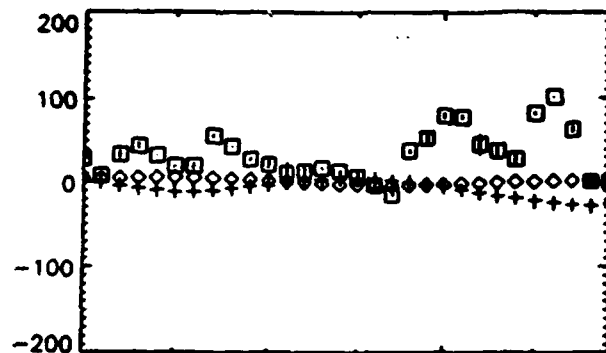
ORBIT = 6565.1  
DATE = 82286

Parameter	51.9	41.7	44.6	58.6	81.2
SZA(deg)	51.9	41.7	44.6	58.6	81.2
GLAT(deg)	-45.7	-19.6	11.5	38.2	68.9



ORBIT = 6681.0  
DATE = 82294

Parameter	46.0	46.6	52.0	60.8	71.8
SZA(deg)	46.0	46.6	52.0	60.8	71.8
GLAT(deg)	-24.5	-6.0	12.3	30.6	48.6



ORBIT = 6604.0  
DATE = 82289

Parameter	44.0	45.4	47.3	57.9	73.2
SZA(deg)	44.0	45.4	47.3	57.9	73.2
GLAT(deg)	-29.3	-11.0	13.4	31.5	55.6

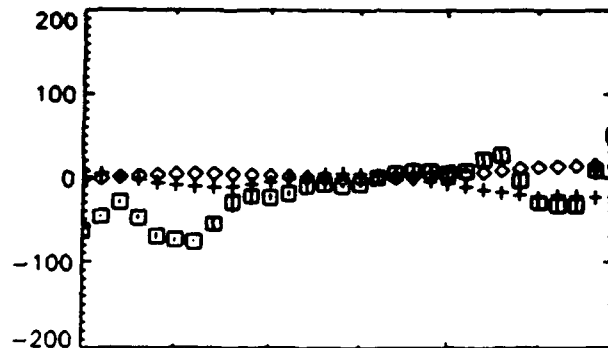


figure 6.4 Three orbits of DE2 showing the surface plot at left and an altitude slice at 110 km. The altitude slice shows the VSH model meridional winds (plusses), the HWM winds (triangles) and the inverted green line winds (boxes).

## CHAPTER 7

### ALTITUDINAL PROFILES

#### 7.1 Red/Green Line Profile Comparisons

During the latter orbits of the DE2 mission the FPI was operated in a dual mode measuring both red line (6300 Å) emissions and green line (5577 Å) emissions during each second of operation. The red line winds can be taken to be true winds at each altitude with no inversion procedure necessary. In this chapter these red line higher altitude winds are stacked upon lower altitude green line winds to test for consistency and/or differences.

Figure 7.1 shows the last six profiles of orbit 8072 with the red line plotted above the solid line at 250 km and the inverted green line winds below. There is a remarkable correlation in the wind speeds at the point where they meet at 250 km. Specifically, profiles 28 and 29 almost have identical red and green line speeds at the junction at 250 km while the other orbits match the wave pattern well. This orbit is during a low period of geomagnetic activity and passes through high latitudes (~65°N to 41°N).

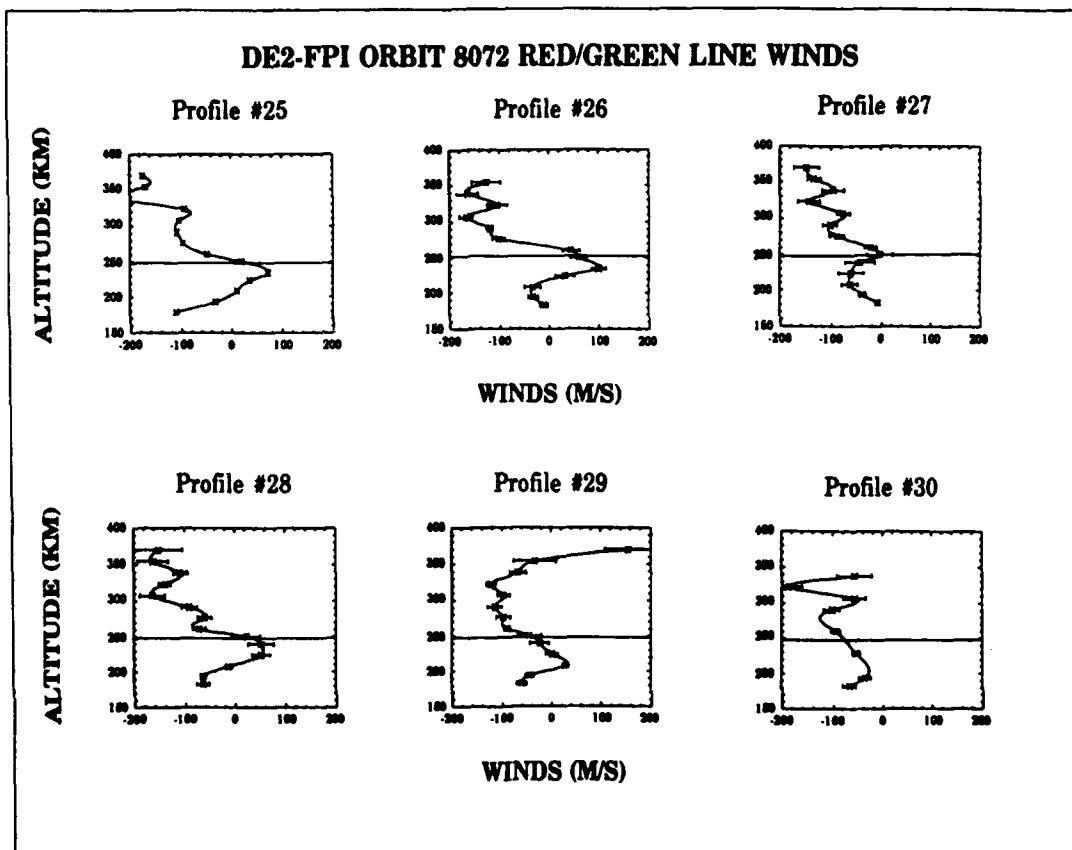


figure 7.1 Six profiles of DE2 orbit 8072 showing red line (6300Å) meridional winds above 250 km and inverted green line meridional winds below 250 km. The points are fitted with a cubic spline interpolation.

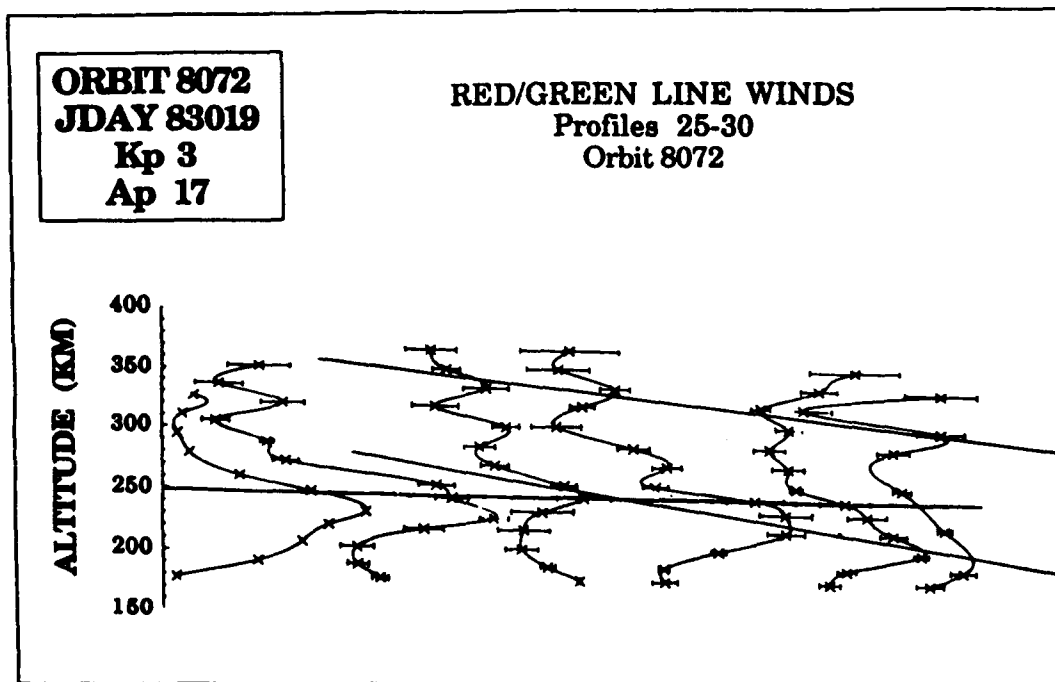


figure 7.2 The same six profiles as in figure 7.1 plotted sequentially. The two straight lines show the downward phase propagation in the wind peaks typical of gravity waves.

Figure 7.2 stacks these profiles next to each other sequentially. The two lines drawn through the peaks in the profiles show a typical downward phase propagation characteristic of gravity waves. It is interesting that this is evident even during a pass through auroral latitudes (since structure tends to become more chaotic there) and across the 250 km red/green line boundary in these plots.

Figures 7.3 and 7.4 similarly show the profiles for DE2 orbit 8092. This orbit passes through the southern auroral region ( $-85^{\circ}$  S to  $-62^{\circ}$  S). The downward phase propagation is not as easy to identify in figure 7.4 for this orbit as it was for orbit 8072, but a case can be made for some wave structure.

An attempt was made to locate an orbit as close to the noon to midnight meridian as possible. The FPI had to be turned off when too close to this track since it would have been looking directly into the sun. Orbit 8088's track was within  $33^{\circ}$  of this meridian and its profiles are shown in figure 7.5. Along this track is where the largest wind speeds should be detected, but here the largest speeds are still only  $\sim 350$  m/s (profile #23). Although these speeds are larger than other orbits presented here, speeds approaching 500 m/s would not be unreasonable. Other orbits should be studied to find greater speeds and to study the associated altitudinal wave structures.

Finally Table 7-1 presents a summary of the latitudinal and altitudinal wavelengths found in the 40 plus orbits processed in this study. These wavelengths agree with those of Nardi (1991) quite well. It is interesting to note that for both the altitudinal and latitudinal waves, the medium Ap orbits showed less deviation than the low Ap orbits. The

reason for this is uncertain and may be only a function of the particular orbits selected for this study.

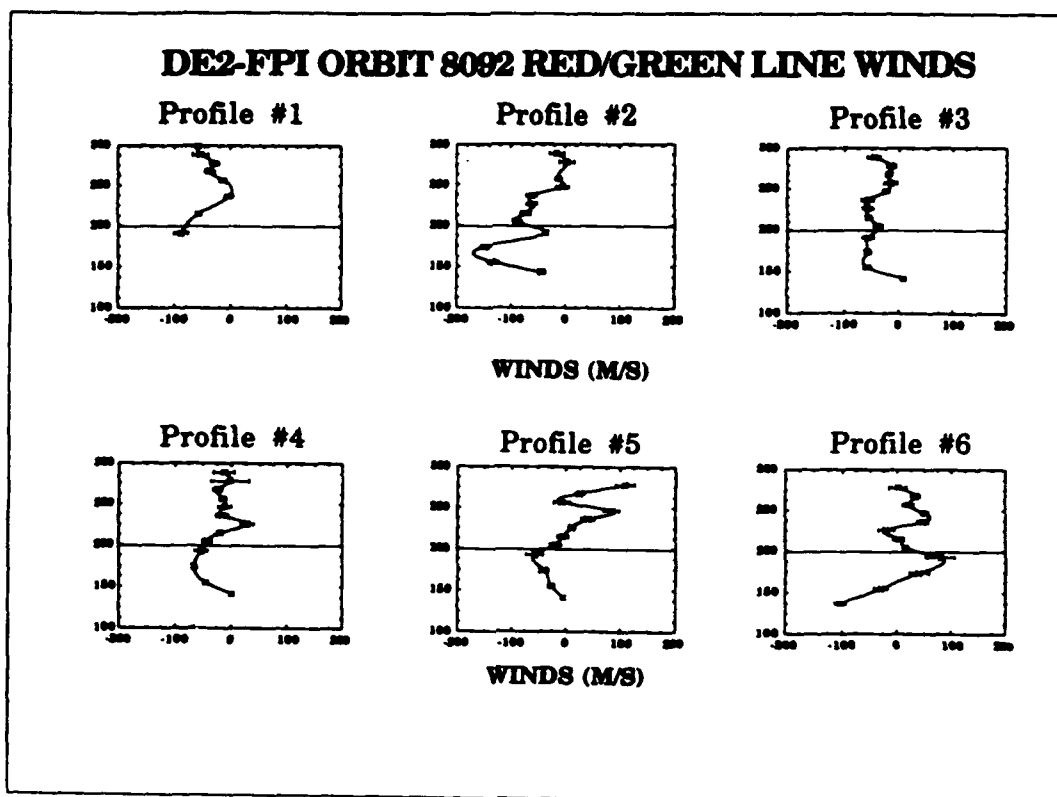


figure 7.3 Six profiles of DE2 orbit 8092 showing red line (6300Å) meridional winds above 200 km and inverted green line winds below 200 km. The points are fitted with a cubic spline interpolation.

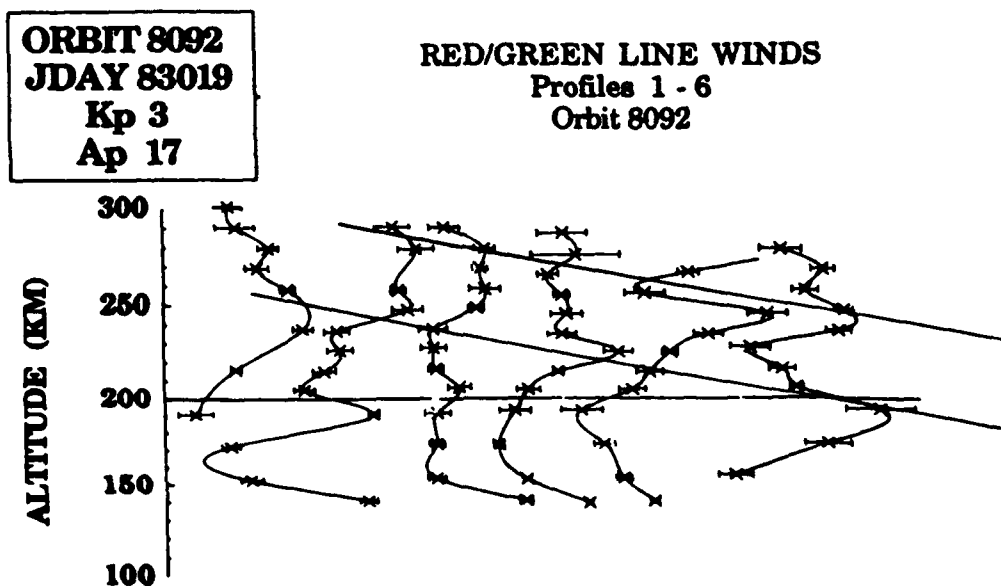


figure 7.4 The same six profiles as in figure 7.3 plotted sequentially. The two straight lines show some downward propagation of wave activity, although not as strongly as orbit 8072.

# DE2-FPI ORBIT 8088 RED/GREEN LINE WINDS

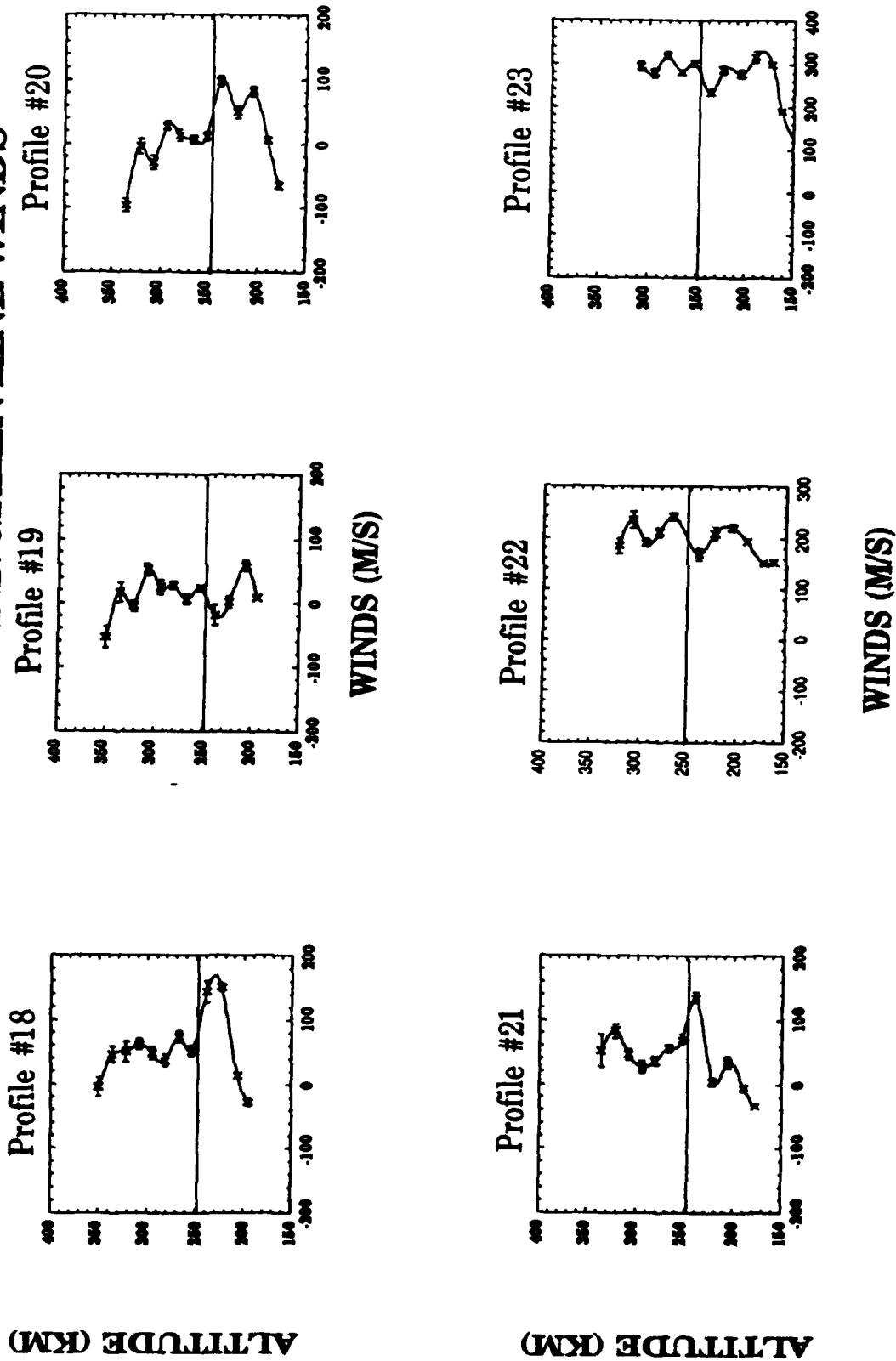


figure 7.5 Six profiles of DE2 orbit 8088. This orbit is as close as the DE2 satellite came to the noon to midnight meridian. Maximum winds here are greater than in dawn to dusk orbits, but still under 400 m/s.

**TABLE 7-1**

**GREENLINE WAVES**  
(INVERTED MERIDIONAL WINDS)

**LATITUDINAL WAVES:**

	<u>Wavelength (degrees Lat)</u>	<u>Standard Deviation (Degrees Lat)</u>
LOW AP (< 20):	12.18	3.88
MED AP (20-40):	10.61	2.80
HIGH AP (>40):	13.51	7.35
OVERALL AVG:	11.92	4.48

---

**ALTITUDINAL WAVES:**

	<u>Average Wavelength</u>	<u>Standard Deviation</u>	<u>Range</u>
LOW AP:	72 km	10 km	62-82 km
MED AP:	73 km	6 km	67-79 km
HIGH AP:	72 km	15 km	57-97 km
OVERALL AVG:	72.3 km	10.3 km	62.3 - 84.6 km

## CHAPTER 8

### DISCUSSION

A wind inversion technique has been developed to recover daytime lower thermospheric meridional winds from satellite measurements of [OI] 5577 Å emissions. A data base of forty-four DE-2 orbits have been processed and analyzed.

An onion peel brightness inversion was used to obtain an inverted volume emission rate from the limb-scanned brightness measurements derived from raw spectrogram data of the DE-2 Fabry-Perot Interferometer. These inverted volume emission rates were then used to apply a least squares fit to Chapman layers to obtain an inverted meridional wind profile.

These inverted winds were compared to the Vector Spherical Harmonic (VSH) Model and the Horizontal Wind Model (HWM). Comparisons to the VSH Model revealed a good correlation at low and mid latitudes with much poorer and variable correlation at high latitudes. Even at low and mid latitudes the VSH model is unable to duplicate the small scale gravity wave effects on the inverted winds, even though the model does incorporate semi-diurnal tides.

The comparisons to the empirical HWM model do not differ significantly with the VSH model comparisons. Once again, the best

correlation is at low and mid latitudes with the poorest correlation at high latitudes.

As with the latitude comparisons, the models fit the data best at low and mid geomagnetic activity indices. For high geomagnetic indices, the correlation is poorer. Interestingly enough, there appears to be a slightly better fit at medium Ap/Kp values than at low Ap/Kp values. The reason for this is uncertain and should be investigated further.

The altitudinal structure of the inverted winds was also examined. The inverted meridional winds revealed much more wave activity than did the line-of-sight winds. Red line derived winds (6300 Å emissions) were stacked on top of the inverted green line emission (5577 Å) and compared. A remarkably good fit occurred between the two profiles at the altitude where they met (200-250 km). This is an encouraging result confirming the strength of the DE-2 FPI data. More wave activity than was expected was found in the red line winds above 250 km.

When stacked sequentially, the profiles show the standard downward propagation of gravity waves. This result appeared even across the meeting point of the red and green line derived winds.

The highest wind speeds revealed in this study were approximately 350 m/s. These speeds occurred when the satellite's track was close to the noon to midnight meridian. Wind speeds as high as 500 m/s may appear, however, in further studies of lower thermospheric winds under active geomagnetic conditions.

Finally, a statistical calculation of the latitudinal and altitudinal wavelengths was conducted. The results confirmed Nardi's (1991) initial results with the latitudinal waves ranging from 10 to 14 degrees of latitude and the altitudinal waves averaging 70 to 75 km.

## **APPENDIX A**

### **A SEARCH FOR EVIDENCE OF IMPACT IONIZATION IN THE ATMOSPHERIC EXPLORER UNIFIED ABSTRACT DATABASE**

#### **A.1 Introduction**

This study investigated the Atmospheric Explorer Satellite (Unified Abstract) database for evidence of impact ionization of neutral species upon contact with the satellite surface. This search is based on a paper by Hanson, Sanatani, and Hoffman (1981) that addressed ionization measurements from the retarding potential analyzer (RPA) and the magnetic ion mass spectrometer (MIMS) on the Atmospheric Explorer Satellites. This initial investigation detected impact ionization or "ion sputtering" from the raw (unaveraged and unprocessed) MIMS and RPA data. Impact ionization occurs when a neutral atom, molecule, or ion strikes a (satellite) surface with sufficient kinetic energy to ionize that particle or an ambient surface particle. Until now, it has been undetermined whether this ionization effect made the transition from the raw data into the Atmospheric Explorer unified abstract database.

## **A.2 Earlier Conclusions**

Hanson, Sanatani, and Hoffman (1981) reported impact ionization resulting in alkali ions  $\text{Na}^+$  and  $\text{K}^+$  and molecular ions  $\text{NO}^+$  and  $\text{O}_2^+$ . These ionizations took place during the night orbits at low altitudes (approximately 150 km).

### **A.2.1 The Magnetic Ion Mass Spectrometer**

The Magnetic Ion Mass Spectrometer (MIMS) measured concentrations of ions from 1 to 64 atomic mass units (amu). The entrance aperture looked radially out from the satellite's equator. Three slits behind the entrance grid separated the ions according to low, mid, or high mass in the mass ratios 1:4:16. These three mass ranges were measured by the instrument at the same time (1 to 4, 4 to 16, and 16 to 64) over a 1 second interval. An alternate mode used a 9 second scan period to and extended the mass range to 90 amu. Figure A-1 is a sketch of the entrance geometry of the MIMS analyzer.

### **A.2.2 Alkali Ions**

In their paper, Hanson et al. [1981] concluded that the source of Na and K atoms could be the ocean salt spray from the launch sites in Florida and California. Several factors support this thesis. First, they suspect that the MIMS entrance grid itself was the main source of  $\text{Na}^+$  and  $\text{K}^+$  since these concentration measurements are heavily dependent on ram angle. Ram angle is the angle between the normal to the entrance grid and the

trajectory of the incoming particle. Therefore a particle entering the instrument at a 90 degree angle to the entrance grid forms a zero degree ram angle and a particle entering from the side of the MIMS forms a large ram angle near 90 degrees. Na and K could have infiltrated into the satellite payload upon takeoff and these deposits would have been upon the MIMS entrance grid wires. Na and K on the front side of the grid wires may have been ionized from collisions of neutral O<sub>2</sub> and N<sub>2</sub> and sputtered away from the MIMS analyzer. This hypothesis agrees with the low measurements of Na<sup>+</sup> and K<sup>+</sup> at low ram angles.

For larger ram angles, larger measurements of Na<sup>+</sup> and K<sup>+</sup> were detected. This may be due to Na and K on the back sides of the wires becoming ionized and sputtering into the MIMS analyzer. The ionized Na and K from the front of the wires (low ram angles) have a better chance of escape from the MIMS since they face away from the instrument than those on the backs of the wires facing into the instrument.

If the Na<sup>+</sup> and K<sup>+</sup> are from ocean salt spray deposits, their lifetimes were not infinite once the satellite was in orbit and removed from the source. The measurements of these ions over the lifetime of the satellite confirms this. The exponential decay time constant is about 500 orbits according to the law:

$$I(n) = I(0) \exp[-n/500]$$

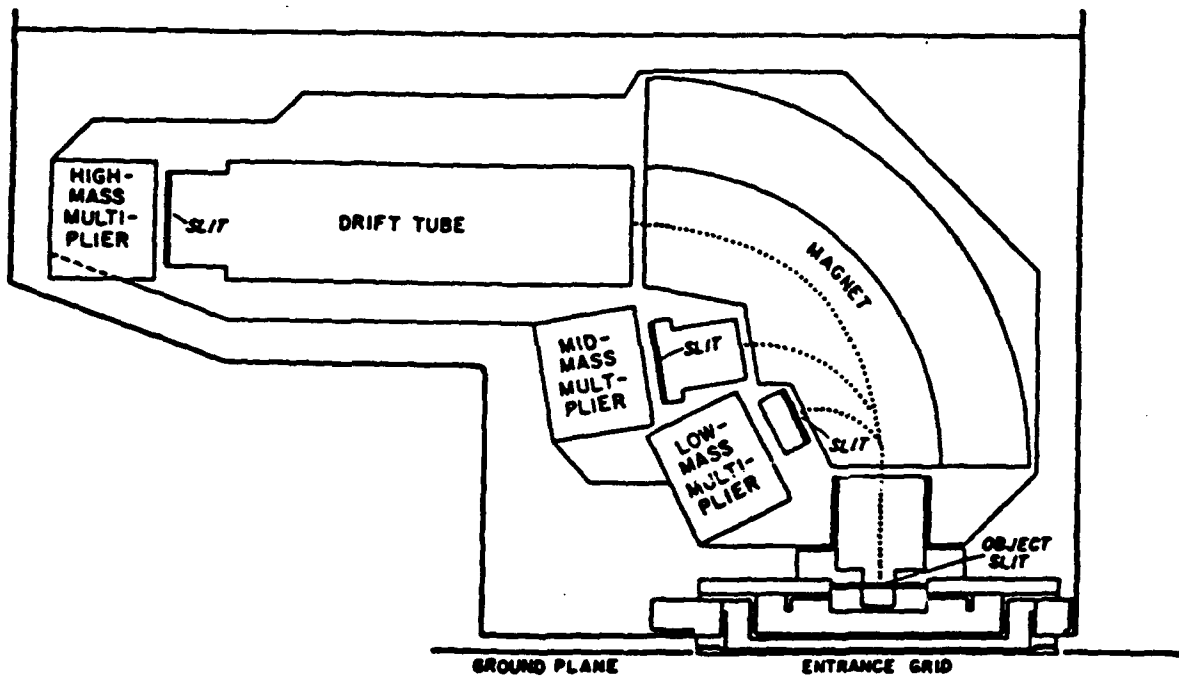


figure A-1 The Magnetic Ion Mass Spectrometer. This drawing shows the entrance grids and slits, the magnet, collector slits, and the electron multipliers. The ion trajectories are shown as dotted lines.  
(NASA, 1987)

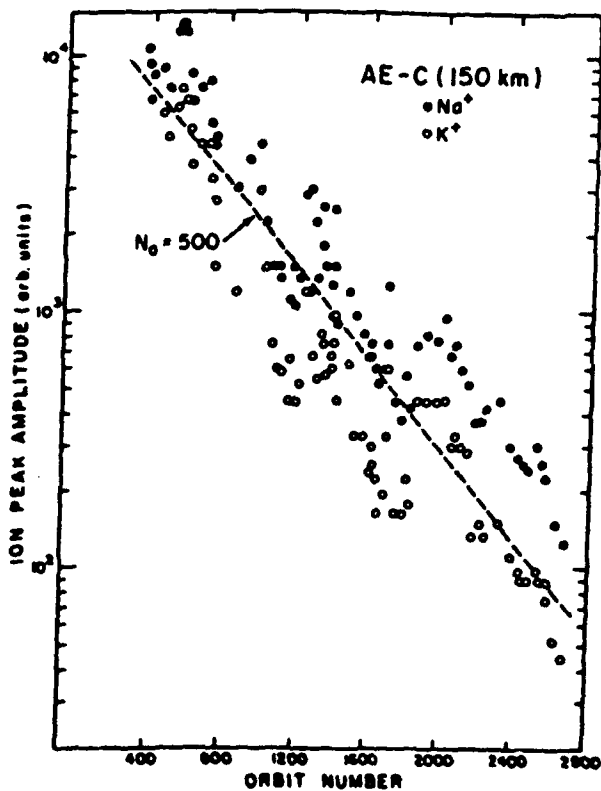


figure A-2 The peak alkali ion current near 150 km as a function of orbit number for AE-C.  
(Hanson et al., 1981)

where  $I(0)$ ,  $I(n)$  are the initial and final concentrations respectively and  $n$  is the orbit number. Figure A-2 shows a plot of this decay for  $\text{Na}^+$  and  $\text{K}^+$ .

What about ambient sources of Na and K (sources at 150 km altitude)? These sources were ruled out due to the lack of ram energy in the mass spectrum measurements and due to the decay of Na and K measurements with time and orbit number.

### A.2.3 Molecular Ions

The molecular ions  $\text{NO}^+$  and  $\text{O}_2^+$  were detected on the mass ion spectrum from the analog AE data with a shift of one atomic mass unit away from the ambient  $\text{NO}^+$  and  $\text{O}_2^+$  due to their lack of ram energy.  $\text{O}_2^+$  displayed a decrease by a factor of  $e$  every 350 orbits similar to the alkali ions.  $\text{NO}^+$  showed a less time dependent decrease, but did decrease with time also (See figure A-3).

The main source of  $\text{O}_2^+$  is from collisions of  $\text{O}_2$  with the satellite surface. The main source of  $\text{NO}^+$  is probably from  $\text{O}^+$  formation from collisions of atomic oxygen with the satellite. Once the  $\text{O}^+$  is formed it combines with a nitrogen atom from the satellite's surface. Where does this surface N atom come from? Possibly from the use of hydrazine as an on board propellant.

There was also no dependence on ram angle for the formation of  $\text{NO}^+$  and  $\text{O}_2^+$ . This is a reasonable result since the sources, ambient O and  $\text{O}_2$ , are not deposits on the entrance grid wires as was the case with Na and K.

#### **A.2.4 Summary**

The efficiency of the impact process is about one ion per  $10^6$   $N_2$  collisions and  $10^5$   $O_2$  collisions, and one ion per  $3 \times 10^3$   $O^+$  collisions. The formation of  $NO^+$  ions is from collisions of  $O$  with the spacecraft surface. The abundance of  $NO^+$  is highly variable due to the extreme variability in the supply of surface nitrogen.

#### **A.3 Effects of Impact Ionization**

None of this would matter if the impact ionization had no effect on the spacecraft or its instruments. The currents produced by these ions, however, did cause problems in the operation of some sensors and in the interpretation of the raw data. If we can better understand and anticipate these currents, we can design instruments to correct for these currents or even use them to assist in the data gathering process.

#### **A.4 The Unified Abstract Atmospheric Explorer Data**

I examined the MIMS  $O_2^+$  number density data to determine whether any of the sputtered ions were evident in the data. Evidence might possibly have shown up in the form of increased number density at approximately 150 km or in any other unusual deviations in the altitude profile at 150 km.

A first guess hinted that all impact ionization would have been filtered out of the UA database since the impact ions had an additional ram

figure A-3 The peak molecular ion current as a function of orbit number for AE-C near 150 km.  
(Hanson et al., 1981)

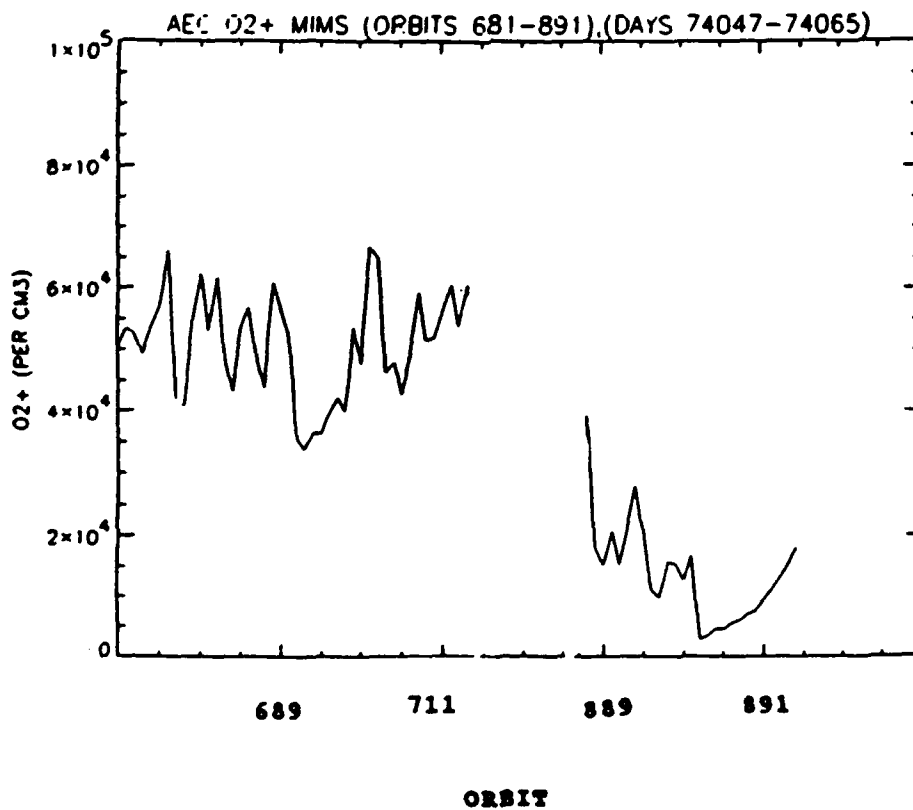
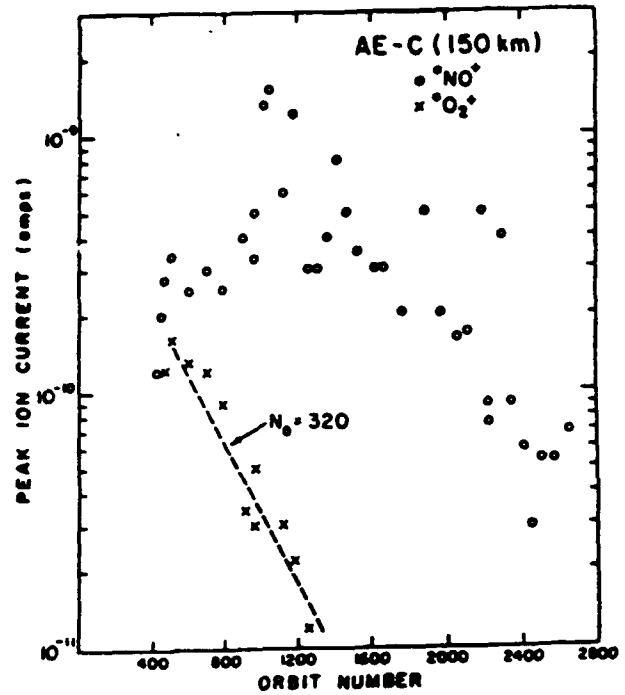


figure A-4 AE-C MIMS O<sub>2</sub><sup>+</sup> number density as a function of orbit number from the UA database. The gap around orbit 725 is where no data was available.

energy that separated them from ambient ions by one atomic mass unit. This indeed proved to be the case. The raw data, however, was not saved and cannot be studied further.

The MIMS  $O_2^+$  was studied from the AE-C satellite. The satellite was in orbit from December 1973 to December 1978. Since the impact ionization was most evident in the first part of the satellite's life, I examined only the first thousand orbits.

Figure A-4 shows a crude plot of  $O_2^+$  number density vs. orbit number. No data was available until Julian day 74026 on the AE-C MIMS  $O_2^+$ . The data displayed represents altitudes from 140 to 160 km. The gap around orbit 711 to 875 is another period where no data was available, but the average values should be decreasing.

The overall decrease is not a reflection of the impact ionization decrease as discussed above, but is simply a reflection of the night side ionospheric decrease as the satellite moves from daytime to nighttime measurements. Even if any impact ionized ions were in this data, separating their decrease with orbit number from the decrease due to the satellite's local solar time would be difficult. In any future data, sputtered ion measurements should be cataloged and stored separately from ambient ions.

## **A.5 Conclusions**

No detectable impact ionization evidence exists in the Unified Abstract Atmospheric Explorer database. Although a negative conclusion, this study does validate the reliability of the MIMS ion data as a true measure of the E region ambient ions. This could be an important

consideration in future models of the lower thermosphere and mesosphere that would include ion number densities.

## REFERENCES

## REFERENCES

- Bates, D.R. (1988a) Recombination in the Normal E and F Layers of the Ionosphere. *Planet. Space Sci.*, 36, 55.
- Bates, D.R. (1988b) Excitation of 557.7 nm OI Line in Nightglow. *Planet. Space Sci.*, 36, 883.
- Bates, D.R. (1988c) Deficiency in Model Ozone in Lower Thermosphere and Excitation of 557.7 nm Nightglow. *Planet. Space Sci.*, 36, 1077.
- Cogger, L. L., Anger, C. D. (1973) The OI 5577 Å Airglow Experiment on the ISIS 2 Satellite, *J. Atmos. Terr. Phys.*, 35, 2081
- Cogger, L. L., Murphree, J. S., Tepley, C. A., Meriwether, J. S. (1985) Measurements of the E Region Neutral Wind Field. *Planet. Space Sci.*, 33, 373.
- Fesen, C. S., Dickinson, R. E., Roble, R. G. (1986) Simulation of Thermospheric Tides at Equinox with the NCAR Thermospheric General Circulation Model, *J. Geophys. Res.*, 91, 4471-4489.
- Greer, R. G. H., Murtagh, D. P., McDade, I. C., Dickinson, P. H. G., Thomas, L., Jenkins, D. B., Stegman, J., Llewellyn, E. J., Witt, G., Mackinnon, J., Williams, E. R. (1986) ETON 1: A Data Base Pertinent to the study of Energy Transfer in the Oxygen Nightglow. *Planet. Space Sci.*, 34, 771.
- Guberman, S. L., (1983) Potential Energy Curves for the Dissociative Recombination from the Proceedings of the N.A.T.O. Advanced Study Institute on Ion-Ion and Electron-Ion Collisions, Baddeck, Nova Scotia. also Physics of Ion-Ion and Electron-Ion Collisions (Edited by Brouillard, F. and McGowan, J.W.) PP. 167-200, Plenum Press, New York.
- Guberman, S. L. (1987) The Production of O(<sup>1</sup>S) From Dissociative Recombination of O<sub>2</sub><sup>+</sup>. *Planet. Space Sci.*, 36, 47.
- Hanson, W. B., Sanatani, S., Hoffman, J. H., (1981) Ion Sputtering From Satellite Surfaces. *J. Geophys. Res.*, 86, 11350-11356.
- Hedin, A. E., Spenser, N. W., Killeen, T. L., (1988) Empirical Global Model of Upper Thermospheric Winds Based on Atmosphere and Dynamics Explorer Satellite Data. *J. Geophys. Res.*, 93, 9959-9978.

- Hedin, A. E., Biondi, M. A., Burnside, R. G., Hernandez, G., Johnson, R. M., Killeen, T. L., Mazaudier, C., Meriwether, J. W., Salah, J. E., Sica, R. J., Smith, R. W., Spenser, N. W., Wickwar, V. B., Viridi, T. S., (1991) Revised Global Model of Thermosphere Winds Using Satellite and Ground-Based Observations. *J. Geophys. Res.*, 96, 7657-7688.
- Hernandez, G. (1971) The Signature Profiles of  $O(^1S)$  in the Airglow. *Planet. Space Sci.*, 19, 467.
- Hoffman, R. A. (1981) Dynamics Explorer. Reprinted from: Space Science Instrumentation, Vol 5, No. 4., D Reidel Publishing Co.
- Killeen, T.L., Hays, P. B. (1981) Nonthermal Line Profiles from  $O(^1S)$  in the Thermospheric Nightglow. *Applied Optics*, 20, 3314
- McDade, L.Lewellyn, E. J., Greer, R. G. H., Witt, G. (1984a) Altitude Dependence of the Vibrational Distribution of  $O_2(c^1\Sigma_u^-)$  in the Nightglow and the Possible Effects of Vibrational Excitation in the Formation  $O(^1S)$ . *Can. J. Phys.*, 62, 780.
- McDade, L.Lewellyn, E. J., (1984b) A comment on Proposed Mechanisms for  $O(^1S)$  in the Aurora. *Planet. Space Sci.*, 32, 1195.
- McDade, L.Lewellyn, E. J., Solheim, B. H. (1985) A Rocket Measurement of  $O(^1S)$  and  $N_2^+$  Emissions in a Pulsating Aurora. *Can. J. Phys.*, 63, 983.
- Nardi, B. (1991) An Inversion Technique to Recover Lower Thermospheric Winds From Space-Borne Remote Measurements of  $[OI] 5577 \text{ \AA}$ . Doctoral Thesis, University of Michigan.
- Sharp, W. E., Torr, D. G. (1979) Determination of the  $O(^1S)$  Production from Coordinated Rocket and Satellite Measurements. *J. Geophys. Res.*, 84, 5345.
- Smith, L. L., Steiger, W. R. (1968) Night Airglow Intensity in the  $[OI] 5577 \text{ \AA}$ ,  $[OI] 6300 \text{ \AA}$ , and  $NaI 5890-96 \text{ \AA}$  Emission Lines. *J. Geophys. Res.*, 73, 2531.
- Solheim, B. H., Llewellyn, E. J. (1979) An Indirect Mechanism for the Production of  $O(^1S)$  in the Aurora. *Planet. Space Sci.*, 27, 473.
- Solomon, S. C., (1987) Tomographic Inversion of Auroral Emissions. Doctoral Thesis, University of Michigan.
- Wallace, L., McElroy, M. B. (1966) The Visual Dayglow. *Planet. Space Sci.*, 14, 677.

- Yau, A. W., Shepherd, G. G. (1979) Energy Transfer from Excited  $N_2$  and  $O_2$  as a source of  $O(^1S)$  in the Aurora. Planet. Space Sci., 27., 481.
- Zipf, E. C., McLaughlin, R.W. (1978) On the Dissociation of Nitrogen by Electron Impact and by E.U.V. Photo-Absorption. Planet. Space Sci., 26,449.
- Zipf, E. C. (1988) The Excitation of  $O(^1S)$  by the Dissociative Recombination of  $O_2^+$  Ions: Electron Temperature Dependence. Planet. Space Sci.,36,621.